

This relation can be verified immediately in Cartesian coordinates for the  $x$ -component:

$$\begin{aligned} (\vec{\omega} \cdot \nabla) u &= \omega_x \frac{\partial u}{\partial x} + \omega_y \frac{\partial u}{\partial y} + \omega_z \frac{\partial u}{\partial z} \\ &= \omega_x \frac{\partial u}{\partial x} + \omega_y \frac{1}{2} \left( \frac{\partial v}{\partial x} + \frac{\partial u}{\partial y} \right) + \omega_z \frac{1}{2} \left( \frac{\partial w}{\partial x} + \frac{\partial u}{\partial z} \right). \end{aligned} \quad (5.11)$$

The  $y$ - and  $z$ -components are expressed correspondingly. Eq. (5.11) can be interpreted physically as the stretching and twisting of vorticity lines. The first term is in the direction of  $\omega_x$  and indicates stretching (which is a change of  $\omega_x$  itself). The other two terms represent twisting to generate  $\omega_x$ .

The appearance of the nonlinear term  $(\vec{\omega} \cdot \nabla) \vec{v}$  in the vorticity-transport equation (5.9) is unique in the sense that it does not occur in the other forms of the Navier-Stokes equations. The term  $(\vec{\omega} \cdot \nabla) \vec{v}$  is responsible for important features in vorticity dynamics that will be outlined in the course of this book. We may add that this term vanishes for two-dimensional flows since  $\vec{\omega} \cdot \nabla \equiv 0$  so that the flow features attributed to it get lost. Therefore, two-dimensional flows can present only an incomplete picture of the vorticity concept.

For general orthogonal coordinates, the components of  $(\vec{\omega} \cdot \nabla) \vec{v}$  are not as easy to obtain as those for Cartesian coordinates. Because of the importance of this term, the components of  $(\vec{\omega} \cdot \nabla) \vec{v}$  are given for both cylindrical polar coordinates and spherical polar coordinates. In cylindrical polar coordinates  $(r, \phi, z)$  they are:

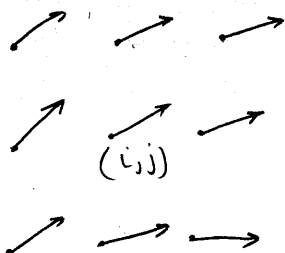
$$\begin{aligned} [(\vec{\omega} \cdot \nabla) \vec{v}]_r &= \omega_r \frac{\partial v_r}{\partial r} + \omega_\phi \left( \frac{1}{r} \frac{\partial v_r}{\partial \phi} - \frac{v_\phi}{r} \right) + \omega_z \frac{\partial v_r}{\partial z}, \\ [(\vec{\omega} \cdot \nabla) \vec{v}]_\phi &= \omega_r \frac{\partial v_\phi}{\partial r} + \omega_\phi \left( \frac{1}{r} \frac{\partial v_\phi}{\partial \phi} + \frac{v_r}{r} \right) + \omega_z \frac{\partial v_\phi}{\partial z}, \\ [(\vec{\omega} \cdot \nabla) \vec{v}]_z &= \omega_r \frac{\partial v_z}{\partial r} + \omega_\phi \frac{1}{r} \frac{\partial v_z}{\partial \phi} + \omega_z \frac{\partial v_z}{\partial z}, \end{aligned} \quad (5.12)$$

and in spherical polar coordinates  $(R, \theta, \lambda)$ :

$$\begin{aligned} [(\vec{\omega} \cdot \nabla) \vec{v}]_R &= \omega_R \frac{\partial v_R}{\partial R} + \omega_\theta \left( \frac{1}{R} \frac{\partial v_R}{\partial \theta} - \frac{v_\theta}{R} \right) + \omega_\lambda \left( \frac{1}{R \sin \theta} \frac{\partial v_R}{\partial \lambda} - \frac{v_\lambda}{R} \right), \\ [(\vec{\omega} \cdot \nabla) \vec{v}]_\theta &= \omega_R \frac{\partial v_\theta}{\partial R} + \omega_\theta \left( \frac{1}{R} \frac{\partial v_\theta}{\partial \theta} + \frac{v_R}{R} \right) + \omega_\lambda \left( \frac{1}{R \sin \theta} \frac{\partial v_\theta}{\partial \lambda} - \frac{v_\lambda}{R} \cot \theta \right), \\ [(\vec{\omega} \cdot \nabla) \vec{v}]_\lambda &= \omega_R \frac{\partial v_\lambda}{\partial R} + \omega_\theta \left( \frac{1}{R} \frac{\partial v_\lambda}{\partial \theta} \right) + \omega_\lambda \left( \frac{1}{R \sin \theta} \frac{\partial v_\lambda}{\partial \lambda} + \frac{v_R}{R} + \frac{v_\theta}{R} \cot \theta \right). \end{aligned} \quad (5.13)$$

Now it is not difficult to write the vorticity equation in those coordinates by using the corresponding parts of the Navier-Stokes equations, given in Section 3.2.

Lugt (1996)

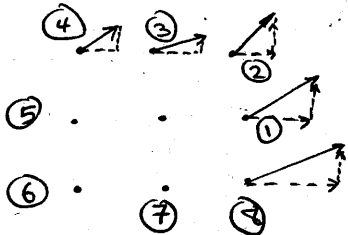


$$\omega_z = \frac{\partial V}{\partial x} - \frac{\partial U}{\partial y}$$

Eff 4

Instead of differentiating the data (i.e. take the difference between discrete numbers), we would get a less noisy result if

We use  $\omega(i,j) = \frac{P}{A} = \frac{\oint \vec{u} \cdot d\vec{l}}{A}$



(We should also)

\* Define a "Vortex line" as a line everywhere having the direction of  $\vec{\omega}$ . (analogous to streamlines which everywhere have the direction of the velocity vector). Lupt calls this "Vorticity Line" and only uses "Vortex Line" when it is an isolated vorticity line in irrotational field. (We won't make this distinction in general; in any case, Vortex line or Vorticity line is descriptive).

In Cartesian coord.

$$\frac{dx}{\omega_x} = \frac{dy}{\omega_y} = \frac{dz}{\omega_z}, \text{ where } \vec{\omega} = \omega_x \hat{i} + \omega_y \hat{j} + \omega_z \hat{k}$$

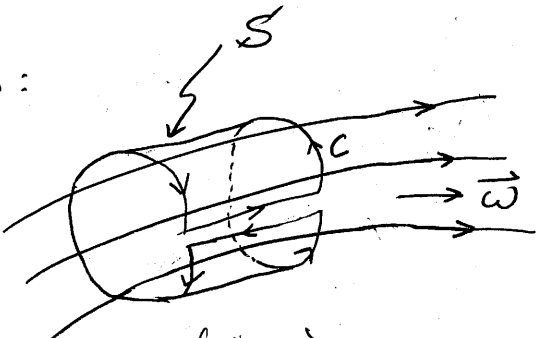
(cf streamline:  $\frac{dx}{u} = \frac{dy}{v} = \frac{dz}{w}$ )

\* A "Vortex tube" is formed when vortex lines pass through a simple closed curve, i.e. a bundle of vortex lines is enclosed in a Vortex tube

\* An isolated Vortex tube encloses a "Vortex filament"

e.g. Rankine vortex is an infinitely long straight Vortex filament

If we apply Stokes theorem to a Vortex tube, with surface S lying along Vortex lines:



thus,  $\vec{\omega} \cdot \vec{n} = 0$  on S, and therefore,  $\oint_C \vec{u} \cdot d\vec{l} = 0$ , i.e. circulation at ends are equal and opposite. Conclude that circulation around a Vortex filament is the same at any cross-section ( $P = \text{constant}$ )

(So we can formally state:)

\*For volume  $V$  formed by  $S'$  and 2 cross sections, net outward flux of vorticity is zero. (One way of stating: Helmholtz's First Theorem)  
i.e. Strength of a vortex is constant along its length  
If volume is very small, using definition of divergence:

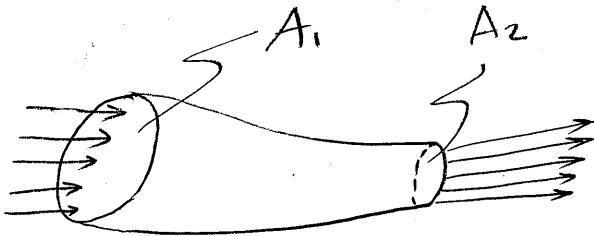
(in 3-d space)  $\operatorname{div} \vec{\omega} = \lim_{V \rightarrow 0} \left( \frac{1}{V} \iint_{\partial V} \vec{\omega} \cdot \vec{n} \, ds \right)$  where  $\delta S$  encloses  $V$

to conclude:

$$\boxed{\operatorname{div} \vec{\omega} = 0}, \text{ i.e. vorticity is always solenoidal}$$

In fact this is a vector identity ( $\operatorname{div}(\operatorname{curl} \vec{A}) = 0$  for any  $\vec{A}$ ). This gives a continuity relation for vorticity like that of velocity of incompressible flow (although the vorticity is solenoidal whether or not the flow is incompressible, i.e. whether or not the velocity is solenoidal)

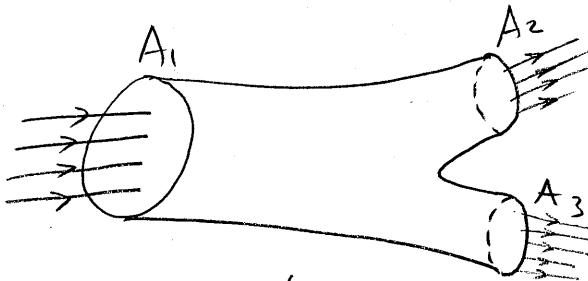
e.g.-



Average over area

$$\overline{\omega} A = \text{const}$$

$$\overline{\omega}_2 = \frac{A_1}{A_2} \overline{\omega}_1 \quad (\text{and})$$



$$\overline{\omega}_1 = \frac{1}{A_1} (\overline{\omega}_2 A_2 + \overline{\omega}_3 A_3)$$

(this also follows from conservation of angular momentum)

(the fact that  $\operatorname{div} \vec{\omega} = 0$  means you can)

\*Conclude that vortex lines can not end in interior of velocity (fluid) field. "Helmholtz's Second Theorem"

Vortex lines (more specifically, vortex tubes) can "end"

only at boundary. However, keep in mind the no-slip condition for a viscous fluid at a solid boundary does not permit a vortex filament to end there either.

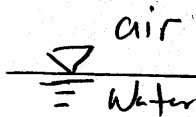


Tornado problem:  
only a singular line ends at the no-slip boundary while the rest of the filament or tube spreads out to a thin sheet

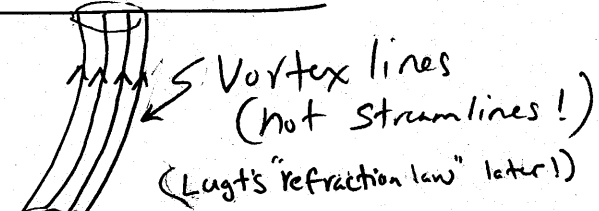
of vorticity. However, a vortex (tube or filament) can end at a free surface

2/1

(in fact, it's not really ending, but continuing in gas)



Note: Helmholtz's 3rd Theorem, which applies to incompressible flows, states that in the absence of rotational external forces, a fluid that is initially irrotational, remains irrotational (much more about vorticity generation & decay later)



(We've seen that if the velocity field is given)  $\vec{U}(\vec{r}, t)$

can determine the corresponding vorticity field:  $\vec{\omega}(\vec{r}, t) \equiv \text{curl } \vec{U}$ .

What about the inverse? (how do we find the velocity induced by vorticity. question is important when you find flow field using vorticity formulation & then seek velocity field)

### Induced Velocity

For incompressible fluid,  $\text{div } \vec{U} = 0$ , hence we can define a

vector potential  $\vec{A}$ , such that

$$\vec{U} \equiv \text{curl } \vec{A} \quad \text{analogous to scalar potential}$$

$$\vec{U} = \text{grad } \phi$$

Since divergence of the curl of any vector is zero,  $\text{div } \vec{U} = 0$  is identically satisfied, thus

$$\begin{aligned} \vec{\omega} &= \text{curl } \vec{U} = \text{curl } \text{curl } \vec{A} \\ &= \text{grad } \text{div } \vec{A} - \vec{\nabla}^2 \vec{A} \end{aligned}$$

but note  $\vec{A}$  is not uniquely defined by  $\vec{U} = \text{curl } \vec{A}$ , since we could always add a gradient, say  $\vec{\nabla} f$  ( $\text{curl } \text{grad } f = 0$ ), we'll choose  $f$  such that  $\text{div } \vec{A} = 0$  (if  $\text{div } \vec{A} \neq 0$ , set  $\vec{A}_2 = \vec{A}_1 + \vec{\nabla} f$  such that  $\vec{\nabla}^2 f = -\text{div } \vec{A}_1$ ).

Thus, take  $\vec{\omega} = -\vec{\nabla}^2 \vec{A}$ . Note it's easiest to consider rectangular coord., so that each component is a Poisson eqn., with  $-w$

Playing role of a source strength.

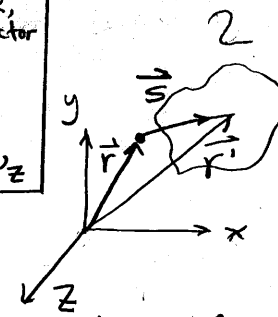
Solution of the vector eqn. is:

$$\vec{A}(\vec{r}, t) = \frac{1}{4\pi} \iiint_V \frac{\vec{\omega}(\vec{r}', t)}{|\vec{r} - \vec{r}'|} dV(\vec{r}')$$

Note: in 2D case,  $\vec{A} = \psi \hat{k}_z$ , where  $\hat{k}_z$  is the unit vector out of the plane, i.e.

$$\frac{\partial \psi}{\partial y} \hat{i} - \frac{\partial \psi}{\partial x} \hat{j} = \vec{u} = \text{curl } \vec{A}$$

$$\text{and } \nabla^2 \psi = \frac{\partial^2 \psi}{\partial x^2} + \frac{\partial^2 \psi}{\partial y^2} = -\omega_z$$



where  $\vec{r}$  is Position Vector of the field

Aside: If you consider the question is  $\text{div } \vec{A} = 0$  in more detail, you find using divergence theorem that  $\text{div } \vec{A} = 0$  if  $\vec{\omega} \cdot \vec{n} = 0$  on boundary. e.g. if boundary is at  $\infty$  and  $\vec{\omega} \neq 0$  only in a finite region, then  $\text{div } \vec{A} = 0$

(if  $\vec{\omega} \cdot \vec{n} \neq 0$  at boundary, (i.e. there is vorticity sticking out), you can introduce a fictitious extension of the flow with  $\vec{\omega} \cdot \vec{n} = 0$  at some surface further away)

(in any case,)

Thus the result:

$$\vec{u} = \text{curl } \vec{A} = -\frac{1}{4\pi} \iiint_V \vec{\omega}(\vec{r}', t) \times \nabla \frac{1}{|\vec{r} - \vec{r}'|} dV$$

(we've used  $\text{curl } f \vec{V} = f \text{curl } \vec{V} + \nabla f \times \vec{V}$ )

This gives:

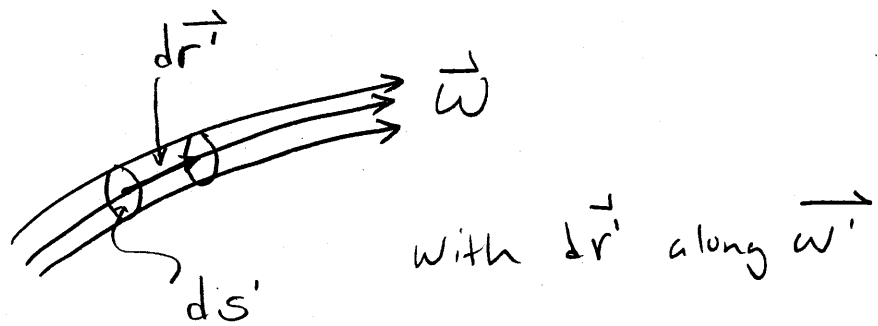
$$\vec{u}(\vec{r}, t) = \frac{1}{4\pi} \iiint_V \frac{\vec{\omega}(\vec{r}', t) \times (\vec{r} - \vec{r}')}{|\vec{r} - \vec{r}'|^3} dV(\vec{r}')$$

Velocity induced by a continuous distribution of vorticity.

(Note: an analogy w/ magnetic field vector  $\vec{H}$  and current density  $\vec{j}$ )

$$\vec{u} \leftrightarrow \vec{H} \quad \vec{\omega} \leftrightarrow \vec{j}$$

To obtain Biot-Savart Law, take vortex tube  
with cross section  $ds'$ ,



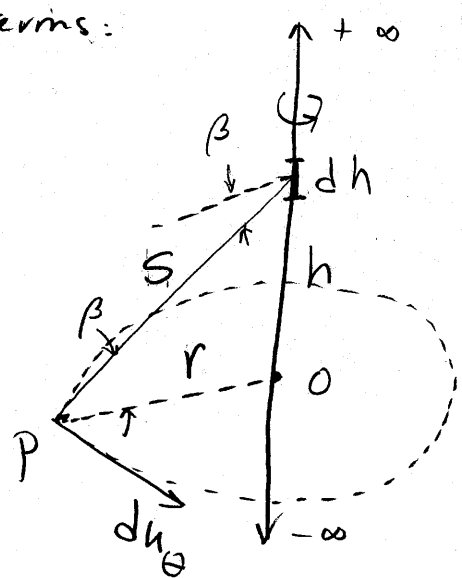
$$\vec{\omega}' dv = \vec{\omega}' ds' |dr'| = \Gamma dr'$$

then

$$\vec{U} = \frac{\Gamma}{4\pi} \iiint \frac{dr' \times (\vec{r} - \vec{r}')}{|\vec{r} - \vec{r}'|^3}$$

Biot-Savart Law  
(Commonly used in  
electromagnetism, as  
well as aerodynamics)

in simpler terms:



(Velocity induced at point P, by a portion  $dh$  of a vortex filament)

(Biot-Savart  
reduces to:)

$$dU_\theta = \frac{\Gamma}{4\pi} \frac{\cos \beta \, dh}{S^2}$$

To find the velocity induced by the entire (rectilinear)  
vortex filament, integrate to find:

$$U_\theta = \frac{\Gamma}{4\pi} \int_{-\infty}^{\infty} \frac{\cos \beta \, dh}{S^2}$$

### 6.6 CROCCO'S THEOREM: A RELATION BETWEEN THE THERMODYNAMICS AND FLUID KINEMATICS OF A COMPRESSIBLE FLOW

Consider again an element of fluid as it moves through a flowfield. The movement of this fluid element is both translational and rotational. The translational motion is denoted by the velocity  $\mathbf{V}$ . The rotational motion is denoted by the angular velocity,  $\boldsymbol{\omega}$ . In any basic fluid mechanic text, it is readily shown that  $\boldsymbol{\omega} = \frac{1}{2}\nabla \times \mathbf{V}$ ; hence the curl of the velocity field at any point is a measure of the rotation of a fluid element at that point. The quantity  $\nabla \times \mathbf{V}$  is itself denoted as the *vorticity* of the fluid; the vorticity is equal to twice the angular velocity.

In this section, we will derive a relationship between the fluid vorticity (a kinematic property of the flow) and the pertinent thermodynamic properties. To begin, consider Euler's equation, Eq. (6.29), without body forces,

$$\rho \frac{D\mathbf{V}}{Dt} = -\nabla p \quad (6.53)$$

Writing out the substantial derivative, Eq. (6.53) is

$$\rho \frac{\partial \mathbf{V}}{\partial t} + \rho(\mathbf{V} \cdot \nabla)\mathbf{V} = -\nabla p \quad (6.54)$$

Recall the combined first and second laws of thermodynamics in the form of Eq. (1.32). In terms of changes in three-dimensional space, the differentials in Eq. (1.32) can be replaced by the gradient operator,

$$T\nabla s = \nabla h - v\nabla p = \nabla h - \frac{\nabla p}{\rho} \quad (6.55)$$

Combining Eqs. (6.54) and (6.55),

$$T\nabla s = \nabla h - \frac{1}{\rho} \left[ -\rho \frac{\partial \mathbf{V}}{\partial t} - \rho(\mathbf{V} \cdot \nabla)\mathbf{V} \right]$$

or

$$T\nabla s = \nabla h + \frac{\partial \mathbf{V}}{\partial t} + (\mathbf{V} \cdot \nabla)\mathbf{V} \quad (6.56)$$

However, from the definition of total enthalpy,

$$h \equiv h_o - \frac{V^2}{2}$$

Hence

$$\nabla h = \nabla h_o - \nabla \left( \frac{V^2}{2} \right) \quad (6.57)$$

Substitute Eq. (6.57) into (6.56):

$$T\nabla s = \nabla h_o - \nabla \left( \frac{V^2}{2} \right) + \frac{\partial \mathbf{V}}{\partial t} + (\mathbf{V} \cdot \nabla)\mathbf{V} \quad (6.58)$$

(from Anderson, Modern Compressible Flow)

Using the vector identity

$$\nabla \left( \frac{V^2}{2} \right) - (\mathbf{V} \cdot \nabla) \mathbf{V} = \mathbf{V} \times (\nabla \times \mathbf{V})$$

Eq. (6.58) becomes

$$T \nabla s = \nabla h_o - \mathbf{V} \times (\nabla \times \mathbf{V}) + \frac{\partial \mathbf{V}}{\partial t} \quad (6.59)$$

Equation (6.59) is called *Crocco's theorem*, because it was first obtained by L. Crocco in 1937 in a paper entitled "Eine neue Stromfunktion fur die Erforschung der Bewegung der Gase mit Rotation," *Z. Angew. Math. Mech.* vol. 17, 1937, pp. 1-7.

For steady flow, Crocco's theorem becomes

$$T \nabla s = \nabla h_o - \mathbf{V} \times (\nabla \times \mathbf{V}) \quad (6.60)$$

Keep in mind that Eqs. (6.59) and (6.60) hold for an inviscid flow with no body forces.

Rearranging Eq. (6.60),

$$\mathbf{V} \times (\nabla \times \mathbf{V}) = \underbrace{\nabla h_o}_{\substack{\text{vorticity} \\ \text{total enthalpy gradient}}} - \underbrace{T \nabla s}_{\substack{\text{gradient of} \\ \text{entropy}}} \quad (6.61)$$

Equation (6.61) has an important physical interpretation. When a steady flowfield has gradients of total enthalpy and/or entropy, Eq. (6.61) dramatically shows that it is *rotational*. This has definite practical consequences in the flow behind a curved shock wave, as sketched in Fig. 4.23. In region 1 ahead of the curved shock, all streamlines in the uniform free stream have the same total enthalpy,  $h_{o1} = h_\infty + V_\infty^2/2$ . Across the stationary shock wave, the total enthalpy does not change; hence, in region 2 behind the shock,  $h_{o2} = h_{o1}$ . Hence, all streamlines in the flow behind the shock have the same total enthalpy; thus, behind the shock,  $\nabla h_o = 0$ . However, in Fig. 4.23 streamline (b) goes through a strong portion of the curved shock and hence experiences a higher entropy increase than streamline (d), which crosses a weaker portion of the shock. Therefore, in region 2,  $\nabla s \neq 0$ . Consequently, from Crocco's theorem as given in Eq. (6.61),  $\mathbf{V} \times (\nabla \times \mathbf{V}) \neq 0$  behind the shock. Thus,

$$\nabla \times \mathbf{V} \neq 0 \quad \text{behind the shock}$$

Hence, Crocco's theorem shows that the *flowfield behind a curved shock is rotational*. This is unfortunate, because rotational flowfields are inherently more

# Experiments on the Richtmyer–Meshkov instability: Wall effects and wave phenomena

M. Brouillette<sup>a)</sup>

Département de génie mécanique, Université de Sherbrooke, Sherbrooke, Québec J1K 2R1, Canada

R. Bonazza

Department of Nuclear Engineering, University of Wisconsin, Madison, Wisconsin 53704

(Received 17 May 1995; accepted 22 January 1999)

Experiments examining the interaction of shock waves with an interface separating two gases of different densities are reported. Flow visualization by the schlieren method and x-ray densitometry reveals that important secondary effects are introduced by the experimental apparatus, especially at the walls of the shock tube from shock wave/boundary layer interaction below, above, and at the interface itself. These effects can impair the observation of the primary phenomenon under study and can lead to the overall deformation of the interface. In particular, the thickness of the viscous boundary layer at the interface is computed using a familiar shock tube turbulent boundary layer model and the occurrence of bifurcation of reflected waves below and above the interface is successfully predicted based on classical bifurcation arguments. The formation of wall vortical structures at the interface is explained in terms of baroclinic vorticity deposition resulting from the interaction of reflected waves with the interface distorted by the boundary layer. This mechanism of wall vortex formation can also explain observed test gas contamination in reflected shock tunnels when shock wave bifurcation is absent. In general, it is found that most of the side effects of the experimental investigation of the Richtmyer–Meshkov instability can be alleviated by performing experiments in large test sections near atmospheric initial pressure. © 1999 American Institute of Physics. [S1070-6631(99)01505-6]

## I. INTRODUCTION

The impulsive acceleration of an interface separating two fluids of different densities can lead to a wide variety of fluid motions. Any perturbation initially present on the interface will be distorted through baroclinic vorticity generation. At the later stages of development of the interface, the interpenetration of the two fluids can generate even more vorticity through the shearing instability.

This class of flows is often referred to as the shock-excited Rayleigh–Taylor instability, or as the Richtmyer–Meshkov instability, for the two scientists who first presented theoretical (Richtmyer<sup>1</sup>) and experimental (Meshkov<sup>2</sup>) results. The past twenty years have seen a strong research interest in this class of problems, because of potential applications mainly in laser implosion of deuterium-tritium nuclear fusion targets and hypervelocity mixing/combustion. Giant steps have been made towards the numerical simulation of these flows, validated with laboratory experiments usually performed in shock tubes.

Shock tube experiments on the Richtmyer–Meshkov instability have been performed in many countries. Agreement between the different results has not been good, owing to the large discrepancy in experimental facilities, diagnostic methods, and test conditions.<sup>3</sup> In fact, the experimental study of interaction of shock waves with an interface between gases of different densities<sup>3–5</sup> has demonstrated that secondary ef-

fects, introduced by the apparatus, can impair the development and observation of the primary phenomenon under study.

The present work describes and classifies the secondary effects that can take place during the experimental investigation of the Richtmyer–Meshkov instability: these have to be understood in order to correctly interpret past and present data and also to assist in planning future experiments. This article is therefore intended as a repertory and guide for experimental and numerical investigators in the field. In particular, the influence of these secondary effects on the interpretation of usual experimental results, such as the measurement of interface turbulent thickening and perturbation growth rates, are discussed. These effects all originate from the repeated interaction of shock waves with the boundary layer developing at the interface. In particular, it is found that the propagation of shock waves over the wall boundary layers can lead to wave bifurcation, and that the interaction of these waves with the distorted interface within the boundary layers causes the formation of a wall vortex which can deform the interface by vorticity-induced strain. It is also found that two- (2D) and three-dimensional (3D) wave fronts are generated by disturbances on the interface and on the side and end walls of the shock tube, and by interaction with the boundary layers. After these waves reverberate between the side and end walls of the shock tube and the interface itself, they are responsible for the introduction of small perturba-

<sup>a)</sup>Electronic mail: martin.brouillette@gme.usherb.ca

tions on the interface, which can explain the observed thickening of initially smooth thick interfaces.

## II. EXPERIMENTAL FACILITY

Using schlieren photography and x-ray densitometry, we study the development of the interfacial instability produced by the interaction of shock and expansion waves parallel to an interface separating two gases of different densities. Experiments are performed in the GALCIT vertical shock tube, where a shock wave is launched from the top of the tube toward the interface located near the bottom end wall. The driven section of the shock tube is square throughout its length, with a 114 mm side, and mates with a test section of the same sectional dimensions; this eliminates the need for the cookie cutter section usually necessary between a round driven section and a square test section. More details about the apparatus, the schlieren flow visualization setup, and the x-ray densitometry system can be obtained from Brouillette<sup>6</sup> and Bonazza.<sup>7</sup>

The experiments are performed with two different kinds of interfaces: (i) a discontinuous interface formed by a thin ( $0.5 \mu\text{m}$ ) nitrocellulose membrane and (ii) a thick, membrane-free, continuous interface smoothed by molecular diffusion, formed by withdrawing a thin (1.2 mm) horizontal metal plate initially separating the gases.

In all cases atmospheric air is used above the interface and helium (He) (density  $0.16 \text{ kg/m}^3$  at  $25^\circ\text{C}$ , 1 atm), carbon dioxide ( $\text{CO}_2$ ) ( $1.8 \text{ kg/m}^3$ ), freon-22 (R-22) ( $3.5 \text{ kg/m}^3$ ), xenon (Xe) ( $5.5 \text{ kg/m}^3$ ), and sulfur hexafluoride ( $\text{SF}_6$ ) ( $6.0 \text{ kg/m}^3$ ), are used below the interface as test gases.

The interface can be installed within the field of view of the flow visualization windows or at two locations (32 or 65 cm) upstream of it. The location of the end wall of the shock tube with respect to the windows can also be moved, allowing us to change the period of the waves reverberating between the interface and the end wall. Although a large number of combinations are possible, two configurations are used: (i) The "short period" experiments are performed with the interface initially in the field of view of the windows, and the end wall of the shock tube is moved just 10 cm downstream of the interface [Fig. 1(a)]. This setup is used to observe the evolution of the interface at early times after the interaction with the incident shock and also to study the effects of multiple impulsive accelerations caused by reverberations of the primary wave between the interface and the end wall of the shock tube. (ii) In the other configuration, the "long period" experiments, the interface is initially located either 32 or 65 cm upstream of the flow visualization windows [Fig. 1(b)]. The end of the shock tube is adjusted so that the first reflection from the end wall interacts with the interface as the latter is near the bottom of the window. Thus, a "snapshot" view of the interface a long time after it interacts with the incident shock, as well as of the effects of the first reshock, are obtained.

For the optical flow visualization setup, the sensitivity of the schlieren system is adjusted so that the interface can easily be distinguished from the image of the shock wave-boundary layer interaction on the observing window. At the

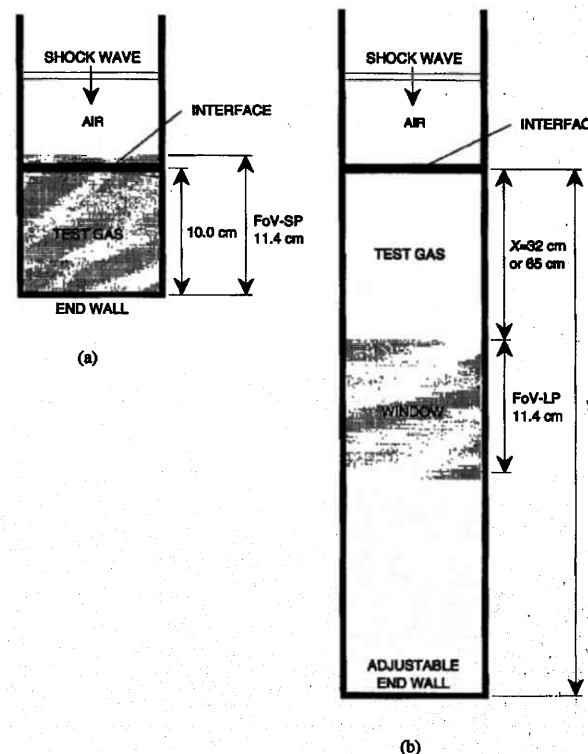


FIG. 1. Experimental configurations. (a) Short period experiments. The interface is initially placed within the field of view of the windows and the end wall of the shock tube is positioned just 10 cm downstream of the initial position of the interface. This setup is used to observe the evolution of the interface at early times after the interaction with the incident shock and also to study the effects of multiple impulsive accelerations caused by reverberations of the primary wave between the interface and the end wall of the shock tube. The field of view of the flow visualization system is indicated by "FoV-SP." (b) Long period experiments. The distance  $X$  between the initial position of the interface and the top of the window can be set to 32 or 65 cm and the distance  $Y$  between the interface and the end wall is adjusted to observe the interaction of the first reshock with the interface as the latter is near the lower end of the window. The field of view of the flow visualization system is indicated by "FoV-LP."

same time, the sensitivity is kept sufficient to record the random field of acoustic waves associated with the shock waves reverberating between the interface and the end of the tube. For examining the fine details of the interaction between the two gases, high-resolution spark schlieren photography is used, which yields one photograph per experimental run. To measure the time evolution of the interface we use high-speed [35 000–60 000 frames per second (fps)] schlieren motion pictures which yield images of lower resolution. To quantify the density field in the interface region, an x-ray flow visualization system is used, with which a single 50 ns flash is produced for each experimental run and an image is recorded by an x-ray negative sandwiched between two fluorescent screens. The x-ray negative is subsequently digitized using a charge-coupled device (CCD) camera and the density field information extracted through a custom image-analysis computer routine.<sup>7</sup>

To perform a run, the sliding plate or membrane is fully inserted into the test section, and the test gas is introduced below the interface. A microprocessor-driven control system is used to provide the sequence for retracting the plate (when

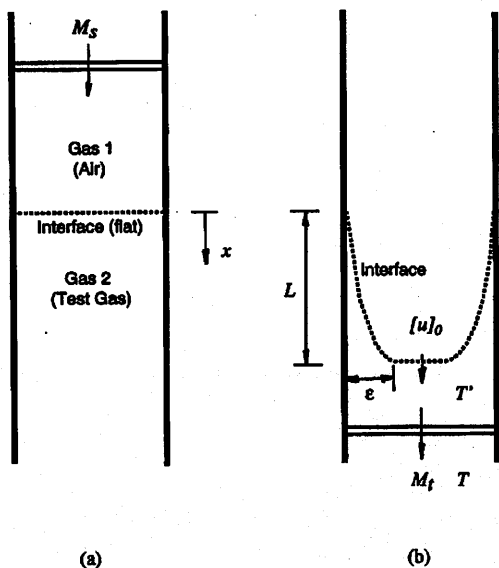


FIG. 3. Development of boundary layer on side walls following the refraction of the incident shock wave at the interface. (a) Initial configuration. (b) Distorted interface in the presence of a viscous boundary layer, whose thickness is  $\epsilon$  at the interface after the latter has travelled a distance  $L$  from its initial position.

action with a  $M_s = 1.32$  incident shock; the interface has travelled 38 cm from its original location. The interface is curved upwards near the wall of the tube under the influence of the boundary layer. The boundary layer thickness can be measured approximately as  $\epsilon \approx 4$  mm from the extent of the curved region on the interface; this is only an estimate since, as the tube is square, the boundary layer is tridimensional in the corners of the tube. A summary of measured values for the thickness of the boundary layer in the test gas, when the interface has traveled to the middle of the observing windows ( $L = 38$  cm) following the refraction of the incident shock for a series of long period experiments, is shown in Table I.

## 2. Computation of boundary layer thickness at the interface

The development of a laminar boundary layer behind a shock wave has been treated by many authors (e.g., Mirels<sup>8</sup>). In the present study, since the pressure (i.e., Reynolds number) is relatively high and the walls of the shock tube are rough, the boundary layers are likely to be turbulent and the analysis of Mirels<sup>9,10</sup> is used.

Mirels' analysis assumes that the compressible turbulent boundary layer behind a shock wave obeys a  $1/7$  power-law velocity profile, and that the gas specific heat ratio  $\gamma$  and Prandtl number  $Pr$  are constant throughout the layer. The latter is a reasonable approximation for the relatively weak shock waves ( $M_s < 1.7$ ) considered in this study. Since the static temperature  $T$  is allowed to vary through the boundary layer, the dynamic viscosity  $\mu$  of the gas is assumed to follow a  $T^{1/2}$  temperature dependence, although it is found that the calculated boundary layer thickness is not very sensitive

TABLE I. Comparison of measured and calculated boundary layer thickness at the interface for long period experiments. Also shown is the predicted occurrence of reshock bifurcation in test gas below the interface and in air above the interface; all experimental observations agree with these predictions of bifurcation. The Atwood ratio  $A_0$  is defined as  $A_0 = (\rho_{\text{test}} - \rho_{\text{air}})/(\rho_{\text{test}} + \rho_{\text{air}})$ , where  $\rho_{\text{air}}$  and  $\rho_{\text{test}}$  designate the initial density of the air and test gas, respectively.

Test gas	$A_0$	$M_s$	$\epsilon$ (mm) @ $L = 38$ cm		Bifurcation of reshock:	
			calculated	measured	in test gas	in air
He	-0.76	1.32	7.8	7	no	yes
		1.48	7.2	6	no	yes
		1.66	6.8	6	no	yes
		1.66 <sup>a</sup>	11.3	9	no	yes
Air	0	1.32	5.5	5	yes	yes
		1.48	5.0	5	yes	yes
		1.66	4.8	5	yes	yes
		0.50	5.0	5	no	no
R-22	0.50	1.12	4.2	5	yes	no
		1.32	3.8	3	yes	no
		1.48	3.5	3	yes	no
		1.66	3.5	3	yes	no
$\text{SF}_6$	0.67	1.12	4.8	4	no	no
		1.32	3.9	4	yes	no
		1.48	3.5	4	yes	no
		1.66 <sup>a</sup>	5.3	4	yes	no

<sup>a</sup> $L = 71$  cm.

to the prescribed viscosity power-law temperature dependence for the shock strengths under consideration here.

Of primary interest is the determination of the boundary layer thickness  $\epsilon$  in the test gas at the interface, after the latter has traveled a distance  $L$  following the arrival of the incident shock (Fig. 3). The expression for  $\epsilon$  in the test gas behind the transmitted shock is given by:

$$\frac{\epsilon}{L} = 0.05745 [0.125 + S(V-1)]^{-4/5} \times \left[ \frac{T'}{T} \right]^{4/5} \left[ \frac{T_m}{T} \right]^{-1/2} \left[ \frac{[u]_0 L}{\nu} \right]^{-1/5}, \quad (1)$$

where

$$V = \left[ 1 - \frac{2}{\gamma+1} \left( \frac{M_t^2 - 1}{M_t^2} \right) \right]^{-1/2} \quad (2a)$$

$$\frac{T_m}{T} = 0.5 \left( 1 + \frac{T'}{T} \right) + 0.22 \left( \frac{T'}{T} \right) \left( \frac{T_r}{T} - 1 \right) \quad (2b)$$

$$\frac{T_r}{T} = 1 + \frac{Pr^{1/3}(V-1)^2}{\frac{\gamma+1}{\gamma-1} V - 1}, \quad (2c)$$

and  $T$  and  $T'$  are the static temperatures in the bulk of the test gas ahead and behind the transmitted shock, respectively,  $T_m$  is the mean temperature in the boundary layer and  $T_r$  is the recovery temperature. The interface velocity imparted by the refraction of the incident shock wave is  $[u]_0$ , and  $\nu$ ,  $\gamma$ , and  $Pr$  are, respectively, the kinematic viscosity, the specific heat ratio, and the Prandtl number in the test gas

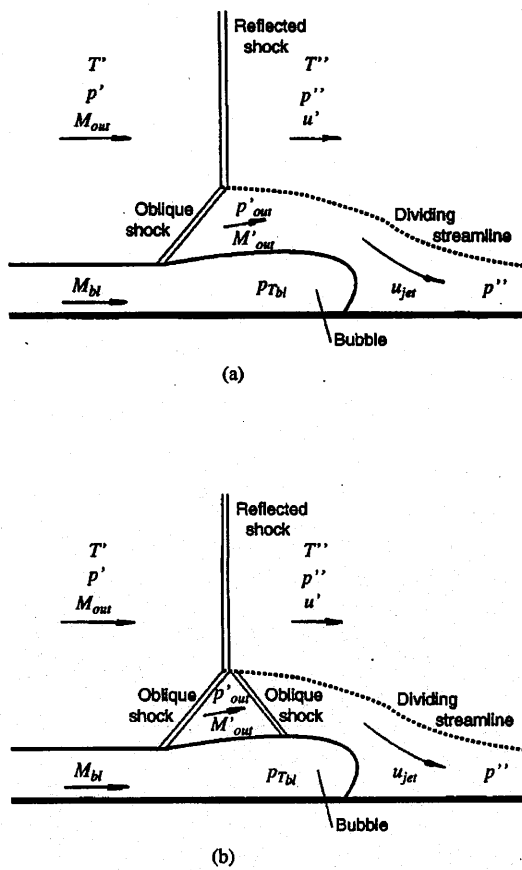


FIG. 6. Shock system over bifurcation bubble in test gas (Mark bubble) in reference frame stationary with reflected shock. (a)  $M'_{out} < 1$ . (b)  $M'_{out} > 1$ .

tinuously under the foot of the reflected shock and into the region behind it. However, for certain values of the transmitted shock Mach number  $M_t$ , it is possible that  $p_{T_{bl}} < p''$ . For this case, a simple steady through flow of the boundary layer fluid cannot be expected. Rather, Mark proposed that this fluid gathers up as a bubble in a region adjacent to the foot of the shock. Assuming that the ratio of specific heats stays constant throughout the boundary layer, Mark calculated that the bubble will appear if the Mach number of the wave incident onto the end wall is within the interval  $1.32 < M_t < 6.45$  for diatomic gases ( $\gamma = 7/5$ ) and within  $1.57 < M_t < 2.80$  for monoatomic gases ( $\gamma = 5/3$ ). A more refined analysis<sup>12</sup> takes into account the possibility for the stagnation pressure minimum to occur within the boundary layer away from the wall, in which case the predicted bifurcation range for monoatomic gases is reduced. This explains the general conception that shock bifurcation can be avoided by using monoatomic gases. Also, since the value of  $\gamma$  in diatomic gases can decrease as a result of the temperature rise across the shock, the interval of bifurcation is effectively increased for these gases. Polyatomic gases, with their low specific heat ratios, have an even larger interval of bifurcation.

In addition, the disturbance produced by the Mark bubble causes at least one oblique shock to form at the base of the reflected wave (Fig. 6). The turning angle of the first

oblique wave can be calculated by assuming that the static pressure  $p'_{out}$  behind it is equal to the stagnation pressure in the bubble  $p_{T_{bl}}$ . If the flow behind this wave is subsonic (i.e.,  $M'_{out} < 1$ ), the necessary increase in pressure after the oblique shock is accomplished by a streamtube area change [Fig. 6(a)]. If  $M'_{out} > 1$ , another oblique shock forms to bring the static pressure up to  $p''$ , the pressure behind the reflected wave [Fig. 6(b)]. Because the flow of the jet over the bubble is processed by one or two oblique shocks as compared to a single normal shock for the flow in the bulk of the fluid, the velocity of the jet  $u_{jet}$  is therefore larger than that of the main flow behind the reflected shock  $u'$ , with a dividing streamline (i.e., a shear layer) separating the two streams.

Table I lists the predicted occurrence of bifurcation of the reshock in the test gas to form a Mark bubble for a series of experiments with He, R-22, SF<sub>6</sub>, and air as test gases. All of these predictions are in agreement with the experimental results.

## 2. Reshock propagation above the interface

The propagation of the reshock above the interface is complicated by the fact that the fluid within the boundary layer does not have the same composition as that outside of it. For the present experiments, the fluid outside the boundary layer above the interface is air and that inside the boundary layer is presumably a mixture of both air and test gas, as discussed before. This difference in composition leads to a mismatch in speed of sounds which can then promote shock bifurcation.

As an example, Fig. 7 shows the propagation of the reshock across an air/He interface for a long period experiment. The result of the interaction of the reshock with the boundary layer at the interface leads to the formation of a complex bifurcated shock system which is trailed by a large bubble. Specifically, since the boundary layer fluid has a higher speed of sound (i.e., it contains helium) than that of the air outside the boundary layer, a precursor wave forms ahead of the transmitted shock.

These flow features can be explained in terms of the so-called Hess<sup>13</sup> bubble. The criteria for the appearance of a bifurcated wave and associated bubble are based on the same pressure-matching arguments as for the Mark bubble, although in this case the first oblique shock over the bubble can be viewed as a precursor wave. In addition, Hess proposed that the jet of fluid over the bifurcation bubble can penetrate into the other fluid across the interface but also possibly back under the boundary layer fluid (Fig. 8). This mechanism has in fact been used to explain the contamination of hot test fluid by cold driver gas in reflected shock tunnels.<sup>14,15</sup>

Figure 9 shows a construction, performed using this approach, for the bifurcation of the first reshock as it crosses an air/He interface ( $M_s = 1.66$ , long period experiment). The actual shape of the bubble cannot be determined exactly with the simple arguments presented above; full numerical simulations<sup>16</sup> have been used to solve this type of problem in more detail. It is seen that there is good agreement between

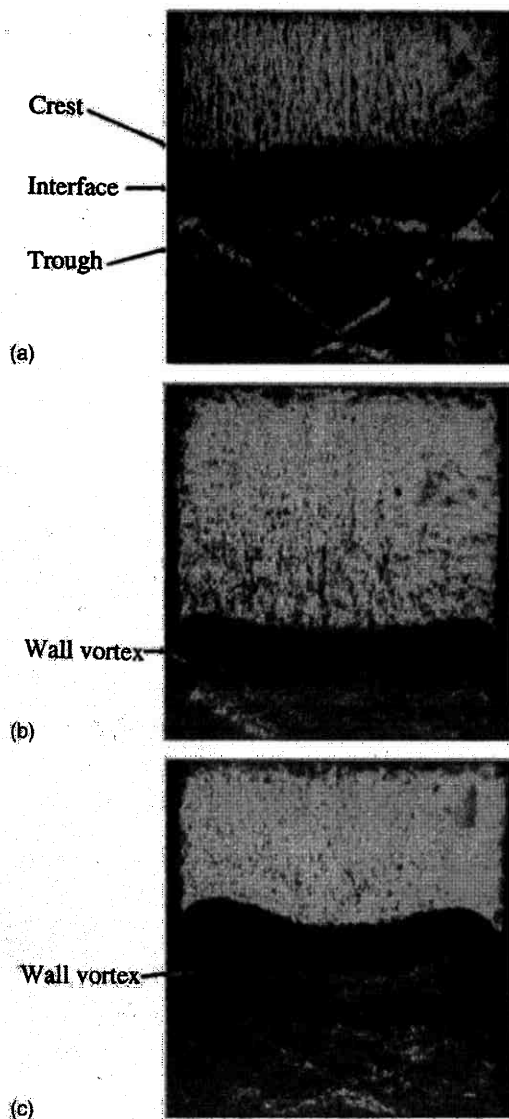


FIG. 10. Richtmyer-Meshkov instability of a plane continuous interface. Air/SF<sub>6</sub>,  $M_s = 1.32$ . Long period experiment. Schlieren photographs from high-speed motion picture. (a)  $t = 3.59$ , (b) 4.39, and (c) 5.19 ms.

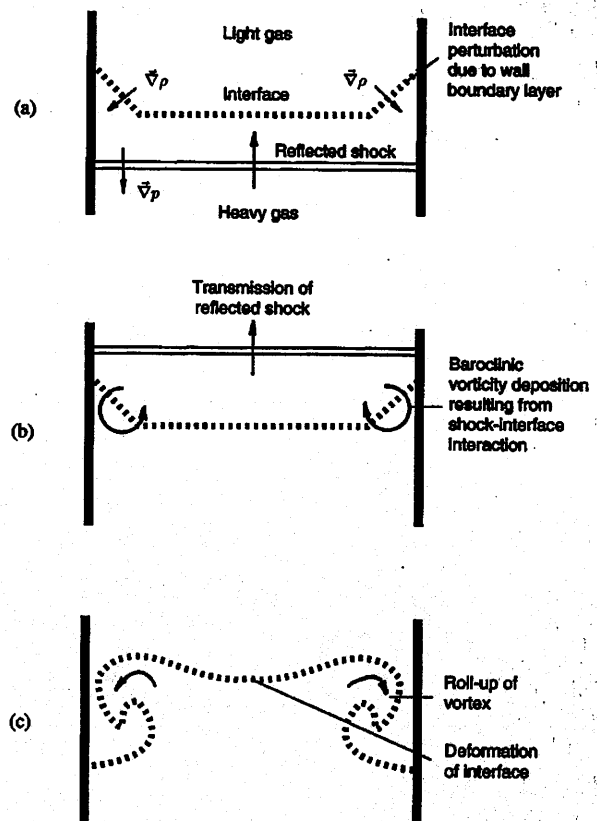


FIG. 12. Mechanism of wall vortex formation on light/heavy interface. (a) Interface perturbation before reshock. (b) Deposition of baroclinic vorticity at interface by reshock. (c) Subsequent roll-up of wall vortex.

interface would be reversed compared to the light/heavy interface. For this case, the interaction of this density gradient with the pressure gradient of the reshock would deposit vorticity in a direction opposite from that shown in Fig. 12(b), and the wall vortex would roll-up in the opposite direction as that shown in Fig. 12(c). However actual results for heavy/light interfaces (cf. Fig. 7) show that the interface is mostly dominated by a large disturbance resulting from the forma-

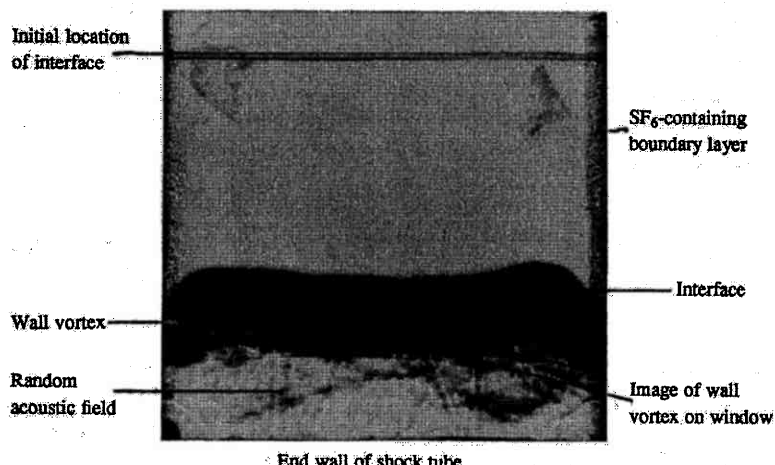


FIG. 11. Richtmyer-Meshkov instability of a plane continuous interface. Air/SF<sub>6</sub>,  $M_s = 1.32$ , short period experiment.  $t = 1.91$  ms. Spark schlieren photograph.

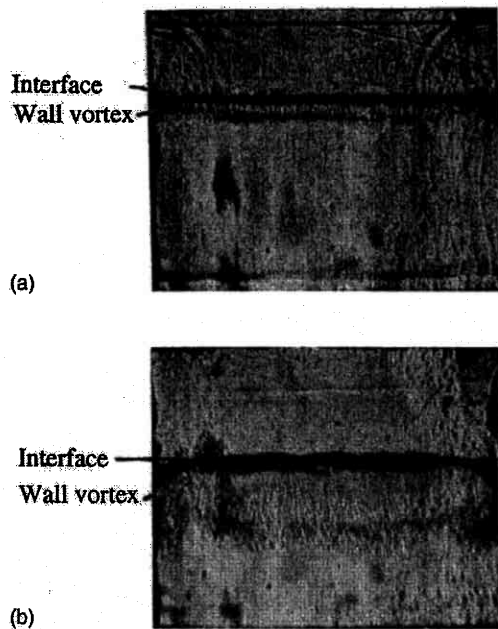


FIG. 14. Richtmyer-Meshkov instability of a plane discontinuous interface. Air/He  $M_s = 1.32$ . Short period experiment. Schlieren photographs from high-speed motion picture. (a)  $t = 0.23$  ms, (b)  $0.63$  ms.

fluid and within the wall boundary layer, with the former probably dominating the latter since the density gradient across the interface is likely to be larger than within the boundary layer, where mixing between the air and test gas is more important [Fig. 13(d)]. As a result of this deposition of vorticity on the interface, the prereshock interface deformation is then amplified, as shown in Fig. 13(e); it should also be noticed that further interaction of the interface with reverberations from the end wall of the test section just repeat and amplify this process, as all reverberations are shocks for the heavy/light case.

An example of this case is shown in Fig. 14 for a short period experiment with an air/helium interface that was initially slightly bulged downwards. For this case the wall vortex develops as the result of repeated interaction with re-shocks reverberating between the interface and the end wall of the tube.

Another case is the light/heavy discontinuous interface that is initially bulged slightly upwards (Fig. 15). For this, the interaction of the incident shock with this interface leads to an increase in the amplitude of the upward bulge. At the same time as the interface propagates down the shock tube and that this bulge grows upwards, the interface is also pulled back on the sides by the action of the wall boundary layer. The resulting perturbation on the interface caused by the combined effect of the bulge and the boundary layer is sketched in Fig. 15(a). Upon the arrival of the reshock, vorticity deposition resulting from interface deformation in the fluid outside the boundary layer dominates, leading to the formation of "reverse" wall vortices [Figs. 15(b) and 15(c)] which roll up in the opposite direction as the vortices on the light/heavy interfaces of Figs. 10 and 11, for which no initial bulge was present.

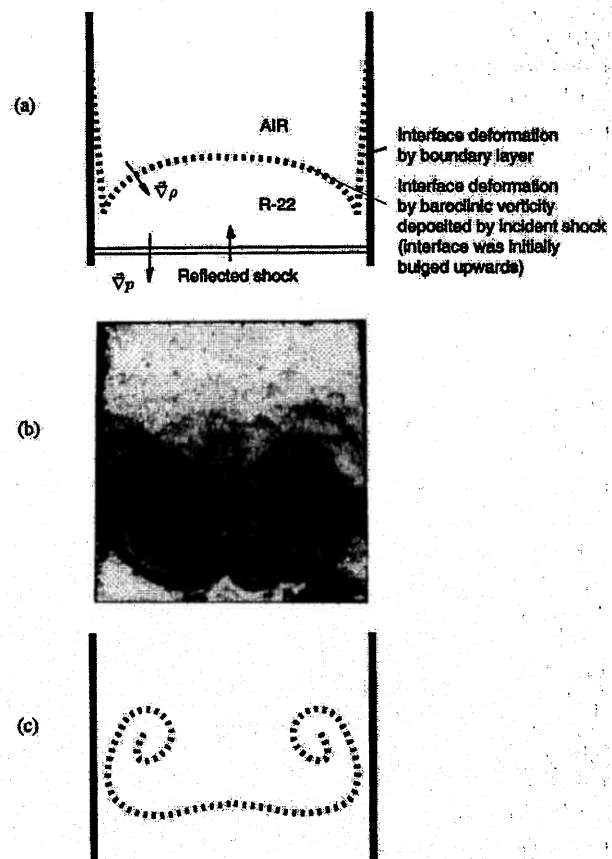


FIG. 15. Reverse wall vortex formation on light/heavy interface with an initial upwards bulge. (a) Deformation of interface after interaction with incident shock. (b) Formation of reverse wall vortex. Air/R-22,  $M_s = 1.32$ , long time configuration. Schlieren photograph from high-speed motion picture. (c) Schematic of reverse wall vortex of (b).

#### IV. WAVE PHENOMENA

This section discusses issues relevant to the wave motions in the experimental observation and data reduction of the Richtmyer-Meshkov instability. In particular, the influence of the plastic membranes on the initial motion of the interface is examined. Also studied are the two- and three-dimensional wave patterns created by the interaction of the planar incident shock wave with a flat interface.

##### A. Acceleration of the membrane at the discontinuous Interface

The effect of the membrane on the refraction of the incident wave at a discontinuous interface can be estimated by considering the influence of the membrane's inertia. The interaction can be analyzed by modeling the membrane as a rigid piston which does not shatter and whose acoustic impedance is large compared to that of the surrounding gases. It is also assumed that the incident wave does not directly transmit through the membrane but that the refraction of the incident shock at the interface produces a constant acceleration  $a = A\Delta p/m$  of the membrane of mass  $m$ , applied until the interface attains its final velocity  $[u]_0$ . The pressure difference across the membrane is  $\Delta p$ , and the cross-sectional

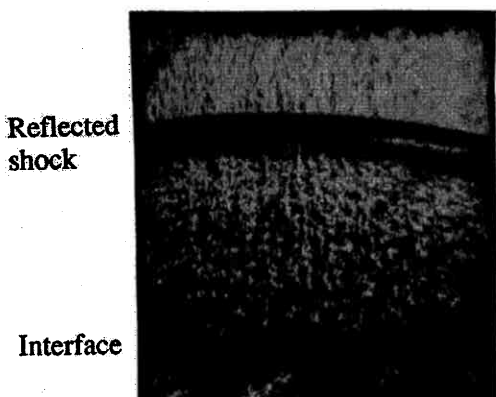


FIG. 17. Richtmyer-Meshkov instability of a plane continuous interface. Air/SF<sub>6</sub>,  $M_s = 1.32$ . Long period experiment,  $t = 4.30$  ms. Schlieren photograph from high-speed motion picture.

presence of small disturbances on the side walls of the tube, such as joints for the plate guide plug and grease left from the edges of the sliding plate, the reflected and transmitted shocks emerging from the interface are accompanied by cylindrical acoustic waves that originate from the wall at the interface. Another wave front also appears on the left side because of the perturbation introduced by the slot into which the plate is retracted. Since the speed of sound is higher in air than in SF<sub>6</sub>, the wave fronts propagate faster above the interface. This leads to the generation of precursor waves below the interface [Fig. 16(b)]. Furthermore, the cylindrical wave in SF<sub>6</sub> propagates faster downstream than the transmitted shock, and the two interact leading to another reflection. Since the angle between the cylindrical wave front and the shock remains constant in time as they propagate downstream, the weak reflected wave is straight and remains at a constant angle. In this case the parameters are such that this reflection comes back to the interface where it meets the wall. Figure 16(c) is a construction for the shocks, the acoustic waves, and their reflections, with the velocities calculated with the simple 1D gas dynamics theory, for the interface of Fig. 16(b) at the same time interval after the interaction with the incident shock. As can be seen, there is good agreement between the experimental and calculated results.

The result of the interaction of the reshock with the boundary layer above the interface is another example of the two dimensionality of the wave pattern even if shock bifurcation is absent. This is because the boundary layer above the interface is composed mainly of test gas and that its local speed of sound differs from that of the air in the bulk of the fluid. After the reshock crosses the interface, the wave transmitted into air has a different velocity than that propagating into the boundary layer. For the light/heavy interface the transmitted shock is bowed upwards, as seen in Fig. 17, because the speed of sound in the boundary layer is lower. For the case of a heavy/light interface, the transmitted shock is preceded by a precursor shock, as seen in Fig. 7.

Also, when the interface velocity is supersonic in the reference frame of the shock tube with respect to one of the gases adjacent to the interface, small disturbances on the walls of the test section cause the appearance of Mach

waves, as seen in Fig. 7(b). For this example, the Mach number of the air flow above the interface is  $M = 1.10$  in the reference frame of the test section, corresponding to a Mach angle of 65°, which agrees with the observed value.

Finally, when the transmitted shock reflects from the end of the shock tube, cylindrical acoustic waves are also generated from the corners at the end of the shock tube because of the disturbance caused by the displacement thickness of the boundary layer.

For short period as well as long period experiments, the reverberation between the end wall and the interface of the trapped waves and their subsequent interaction produces three-dimensional wave patterns. The end result of this is the randomization of the wave field below the interface, as shown in Figs. 10(c) and 11. The interaction of these waves with the interface is the suggested mechanism for introducing perturbations on the smooth continuous interfaces, the growth of which has been the subject of previous investigation.<sup>3,4,19</sup>

## V. DISCUSSION

### A. Effect of reduced initial pressure

Equation (1) shows that the turbulent boundary layer thickness in the test gas at the interface varies as  $\epsilon_{\text{turb}} \sim [u]_0^{-1/5} L^{4/5} / \nu^{-1/5}$ , but since  $\nu = \mu/p$  and  $p \sim \rho/T$ , it follows that, for a given initial temperature  $T$ ,  $\epsilon_{\text{turb}} \sim p^{-1/5}$ ; for a laminar boundary layer, which would be present for the case of smooth walls and/or low initial test pressure, this power law dependence would become  $\epsilon_{\text{laminar}} \sim p^{-1/2}$ . These relationships show that reducing the initial test pressure significantly increases the boundary layer thickness at the interface. In particular, all other parameters remaining constant, performing the experiments at initial pressures of  $p = 0.1, 0.01$ , and  $0.001$  atm, for example, would increase the turbulent boundary layer thickness at the interface by factors 1.6, 2.5, and 4.0, respectively, with respect to experiments at atmospheric conditions; for a laminar boundary layer at these pressures, this thickness would be increased by factors of 3.2, 10, and 31, respectively, over experiments performed at 1 atm. For the present experimental facility, this would mean that reducing the initial pressure in the test section, for example to increase the incident shock Mach number, could produce boundary layers at the interface which could occupy up to 50% of the width of the test section; this would certainly have a severe influence on the development of the instability at the interface. In particular, this argument explains the highly distorted shape of interfaces observed by Houas *et al.*<sup>18</sup> in their experimental study of the Richtmyer-Meshkov instability performed at low pressure (0.015 atm) with a narrow test section (8.5 cm square section).

Large boundary layers not only influence the natural development of the instability at the interface following the refraction of the incident shock, but greatly modify the extent of the shock-boundary layer region after the first and subsequent reshocks. In particular, it is generally agreed that the width of the Mark or Hess bubbles resulting from shock bifurcation scales directly with the thickness of the boundary layer at the interface (e.g., Fig. 4), and the present results

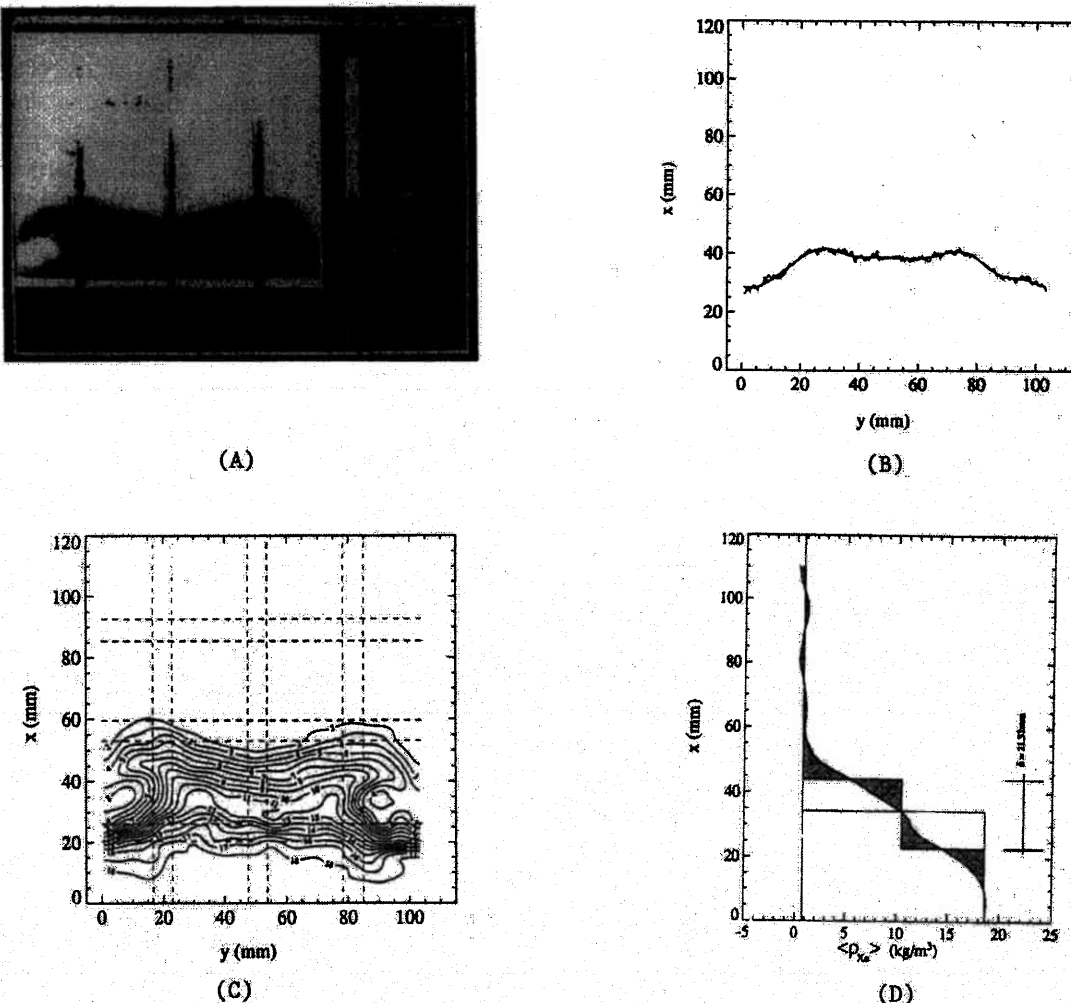


FIG. 18. Richtmyer-Meshkov instability of a plane continuous interface. Air/xenon,  $M_s = 1.33$ . Long period experiment,  $t = 5.82$  ms. (a) Optical density of radiograph. (b) Mean interface shape. (c) Density contours (labeled in  $\text{kg}/\text{m}^3$ ). (d) Average density profile.

feature of the air/air interfaces is that the membrane did not appear to shatter upon wave refraction at the interface. If this were the case for discontinuous interfaces formed between dissimilar gases, the membranes would have a strong growth-impairing effect; there is no experimental evidence, however, that the membrane does not shatter when the Richtmyer-Meshkov instability is present. Experiments performed at high incident shock Mach numbers would clear this uncertainty as the temperatures generated by the waves could be sufficient to vaporize the plastic membrane.<sup>26</sup>

The development of vortices on the side walls of the test section can seriously modify the thickening of the interfaces caused by the Richtmyer-Meshkov instability in the bulk of the fluid. In particular, the velocity field induced by the wall vortices stretches the interface which causes a reduction in its apparent rate of turbulent thickening. The magnitude of this effect can be estimated by computing the strain field associated with two incompressible line vortices each positioned a distance  $D$  from an infinite vertical side wall (Fig. 19). Since the system is periodic in the  $y$  direction,<sup>27</sup> the

strain rate  $\dot{s}$  produced in the middle of the test section ( $y = W/2$ ) by these two vortices is given by:

$$\dot{s} = \frac{2\pi\Gamma}{W^2} \frac{\sinh\left(\frac{2\pi x}{W}\right) \sin\left(\frac{2\pi D}{W}\right)}{\left[\cosh\left(\frac{2\pi x}{W}\right) + \cos\left(\frac{2\pi D}{W}\right)\right]^2}, \quad (4)$$

where  $\Gamma$  and  $W$  are, respectively, the circulation of each vortex and the width of the test section. The strain rate in the middle of the test section can thus be calculated for any axial location  $x$  given the value of  $D$  and  $\Gamma$ .

For example, for a long period experiment performed with a continuous air/SF<sub>6</sub> interface and  $M_s = 1.32$  (Fig. 10), the location of the wall vortices at  $t = 5.19$  ms is at  $D = 10$  mm and the middle of the interface is at  $x = -0.20$  mm with respect to the wall vortices. The circulation  $\Gamma$  can be estimated by evaluating the tangential velocity  $u_t$  of the roll-up of the vortex from  $\Gamma \approx 2\pi u_t R$ , where  $R$  is the radius of the vortex. For this particular case,  $u_t \approx 10$  m/s and  $R \approx 10$  mm,

positive), the wall vortex can ultimately contaminate the entire test gas slug by making its way to the end wall of the shock tube. The large scatter in the results does not allow specific conclusions to be drawn with regards to the effect of shock Mach number or interface thickness and this is due mostly to the large uncertainty in tracking the extent of the wall vortex.

### E. Small-scale perturbations on initially smooth interfaces

It is also found that 2D and 3D wave fronts are generated by disturbances on the interface and on the side and end walls of the shock tube, and by interaction with the boundary layers. After these waves reverberate between the side and end walls of the shock tube and the interface itself, they can be responsible for the introduction of small perturbations on the interface, which can explain the observed thickening of initially smooth thick interfaces.<sup>3,4,19</sup> These effects have to be kept in mind when comparing results from experiments performed in different facilities, where the geometry and experimental conditions are not the same.

## VI. CONCLUSIONS

The development of viscous boundary layers on the side walls of the shock tube in the fluid in motion behind the incident shock wave can cause the bifurcation of the reflected waves and thereafter the formation of wall bubbles and interface-contaminating jets. The appearance of these bifurcation wave patterns has been observed in the context of the Richtmyer-Meshkov instability and there were successfully compared with the models of Mark and Hess. The generation of vortical structures by shock wave-boundary layer interaction at the interface has also been demonstrated. Even if wave bifurcation arguments preclude the appearance of interface penetration jets, significant contamination can be caused by the wall vortex mechanism. The need for experimental methods to distinguish the effects of these wall vortices from the primary phenomena under study has also been pointed out. Moreover, the strain field induced by the vorticity in these wall structures tends to thin the interface; the magnitude of this effect in most of the present experiments is estimated to be of order 10% for discontinuous interfaces and 50% for continuous interfaces. The accurate characterization of interface phenomena requires the identification of extraneous effects introduced by the experimental apparatus. This could be achieved more easily by using different flow visualization and measurement techniques. The comparison of results obtained from different facilities, where the geometry and experimental conditions are not the same, is difficult to achieve, since the accurate quantification of most of these effects is not yet achievable. In general, it can be concluded that most of the side effects of the experimental investigation of the Richtmyer-Meshkov instability can be alleviated by performing experiments in large test sections at near atmospheric initial pressure.

- <sup>1</sup>R. D. Richtmyer, "Taylor instability in shock acceleration of compressible fluids," *Commun. Pure Appl. Math.* **8**, 297 (1960).
- <sup>2</sup>E. E. Meshkov, "Instability of the interface of two gases accelerated by a shock wave," *Sov. Fluid Dynamics* **4**, 101 (1969).
- <sup>3</sup>M. Brouillette and B. Sturtevant, "Growth induced by multiple shock waves normally incident on plane gaseous interfaces," *Physica D* **37**, 248 (1989).
- <sup>4</sup>M. Brouillette and B. Sturtevant, "Experiments on the Richtmyer-Meshkov instability: Small-scale perturbations on a plane interface," *Phys. Fluids A* **5**, 916 (1993).
- <sup>5</sup>M. Brouillette and B. Sturtevant, "Experiments on the Richtmyer-Meshkov instability: Single-scale perturbations on a continuous interface," *J. Fluid Mech.* **263**, 271 (1994).
- <sup>6</sup>M. Brouillette, Ph.D. thesis, California Institute of Technology, 1989.
- <sup>7</sup>R. Bonazza, Ph.D. thesis, California Institute of Technology, 1992.
- <sup>8</sup>H. Mirels, NACA TN-3401 (1955).
- <sup>9</sup>H. Mirels, "Shock tube test time limitation due to turbulent-wall boundary layer," *AIAA J.* **2**, 84 (1964).
- <sup>10</sup>H. Mirels, "Turbulent boundary layer behind constant velocity shock including wall blowing effects," *AIAA J.* **22**, 1042 (1983).
- <sup>11</sup>H. Mark, "The interaction of a reflected shock wave with the boundary layer in a shock tube," *J. Aeronaut. Sci.* **24**, 304 (1957).
- <sup>12</sup>S. Byron and N. Rott, "On the interaction of the reflected shock wave with the laminar boundary layer on the shock tube walls," in *Proceedings of the 1961 Heat Transfer and Fluid Mechanics Institute* (Stanford University Press, Standford, California, 1961), p. 38.
- <sup>13</sup>R. V. Hess, "Interaction of moving shocks and hot layers," *NACA TN-4002* (1957).
- <sup>14</sup>L. Davies and J. L. Wilson, "Influence of reflected shock and boundary-layer interaction on shock-tube flows," *Phys. Fluids* **12**, 37 (1969).
- <sup>15</sup>R. J. Stalker and K. C. A. Crane, "Driver gas contamination in a high-enthalpy reflected shock tunnel," *AIAA J.* **16**, 277 (1978).
- <sup>16</sup>W. J. Glowacki, A. L. Kuhl, H. M. Glaz, and R. E. Ferguson, "Shock wave interaction with high sound speed layer," in *Shock Waves and Shock Tubes*, edited by D. Bershader and R. Hanson (Stanford University Press, Stanford, 1986), p. 188.
- <sup>17</sup>P. A. Thompson, *Compressible-Fluid Dynamics* (McGraw-Hill, New York, 1972).
- <sup>18</sup>L. Houas, A. Farhat, and R. Brun, "Shock induced Rayleigh-Taylor instability in the presence of a boundary layer," *Phys. Fluids* **31**, 807 (1988).
- <sup>19</sup>G. Rodriguez, I. Galametz, H. Croso, and J.-F. Haas, "Richtmyer-Meshkov instability in a vertical shock tube," in *Shock Waves@Marseille IV, Proceedings of the 19th International Symposium on Shock Waves*, edited by R. Brun and L. Dumitrescu (Springer, New York, 1995), p. 275.
- <sup>20</sup>M. Vetter and B. Sturtevant, "Experiments on the Richtmyer-Meshkov instability of an air/SF<sub>6</sub> interface," *Shock Waves* **4**, 247 (1995).
- <sup>21</sup>R. Bonazza and B. Sturtevant, "X-ray measurements of growth rates at a gas interface accelerated by shock waves," *Phys. Fluids* **8**, 2496 (1996).
- <sup>22</sup>J. W. Jacobs, "Shock-induced mixing of a light-gas cylinder," *J. Fluid Mech.* **234**, 629 (1992).
- <sup>23</sup>J. M. Budzinski, R. F. Benjamin, and J. W. Jacobs, "Influence of initial conditions on the flow patterns of a shock-accelerated thin fluid layer," *Phys. Fluids* **6**, 3510 (1994).
- <sup>24</sup>A. I. Abamukov, V. Yu. Fadeev, S. I. Kholkin, E. E. Meshkov, V. V. Nikiforov, P. N. Nizovtsev, N. N. Sadilov, S. K. Sobolev, V. A. Tilkunov, V. O. Tochilin, A. I. Tolshmyakov, and N. V. Zhidov, "Studies of film effects on the turbulent mixing zone evolution in shock tube experiments," in *Proceedings of the Fifth International Workshop on Compressible Turbulent Mixing*, edited by R. Young, J. Glimm, and B. Boston (World Scientific, Singapore, 1996), p. 118.
- <sup>25</sup>M. V. Bliznetsov, Y. V. Vlasov, V. I. Dudin, E. E. Meshkov, A. A. Nikulin, V. A. Til'kunov, A. I. Tolshmyakov, and S. A. Kholkin, "How the film may control the gas-gas turbulent mixing development in shock tube experiments," in *Proceedings of the Sixth International Workshop on Compressible Turbulent Mixing*, edited by G. Jourdan and L. Houas (Imprimerie Caractère, Marseille, 1997), p. 90.
- <sup>26</sup>S. G. Zaitsev, E. V. Lazareva, V. V. Chernukha, and V. M. Belyaev, "Intensification of mixing at the interface between media of different densities upon the passage of a shock wave through it," *Sov. Phys. Dokl.* **30**, 579 (1985).
- <sup>27</sup>L. Rosenhead, "The formation of vortices from a surface of discontinuity," *Proc. R. Soc. London, Ser. A* **134**, 170 (1931).

Substitute  $S = r \sec \beta$  and  $h = r \tan \beta$

1/17

into integral and integrate w.r.t.  $\beta$  between  $\pm \frac{\pi}{2}$ ,

find:

$$U_\theta = \frac{P}{2\pi r}$$

Which is precisely the velocity induced at P arising from a point vortex at the origin in a two-dimensional flow.

Transport equations for  $\vec{\omega}$  and  $T$ , i.e.  $\frac{D\vec{\omega}}{Dt}$  and  $\frac{DT}{Dt}$

Navier-Stokes eqn: (in vector form)  $\frac{\partial \vec{u}}{\partial t} + (\vec{u} \cdot \nabla) \vec{u} = -\frac{1}{\rho} \nabla p + \gamma \nabla^2 \vec{u}$

Using vector identity:  $\text{grad}(\vec{u} \cdot \vec{v}) = (\vec{u} \cdot \nabla) \vec{v} + (\vec{v} \cdot \nabla) \vec{u} + (\vec{u} \times (\nabla \times \vec{v})) + (\vec{v} \times (\nabla \times \vec{u}))$

$$\Rightarrow \frac{1}{2} \nabla(\vec{u}^2) = (\vec{u} \cdot \nabla) \vec{u} + \vec{u} \times \underbrace{(\nabla \times \vec{u})}_{\vec{\omega}}$$

N-S eqn. becomes:

$$\frac{\partial \vec{u}}{\partial t} + \nabla\left(\frac{1}{2} \vec{u}^2\right) - \vec{u} \times \vec{\omega} = -\frac{1}{\rho} \nabla p + \gamma \nabla^2 \vec{u}$$

Vorticity transport eqn. can be derived by taking curl of the momentum eqn.:

$$\nabla \times \left\{ \frac{\partial \vec{u}}{\partial t} + \vec{u} \times \vec{\omega} \right\} = \left( -\frac{1}{\rho} = \text{const} \Rightarrow \text{curl } -\frac{1}{\rho} \nabla p = 0 \right)$$

0 (curl of gradient = 0)

$$\frac{\partial \vec{\omega}}{\partial t} - \nabla \times (\vec{u} \times \vec{\omega}) = \gamma \nabla^2 \vec{\omega}, \quad \text{where } \vec{\omega} = \frac{\text{Vorticity}}{\text{Vector}} = \text{curl } \vec{u}$$

Use vector identity:  $\nabla \times (\vec{u} \times \vec{\omega}) = \vec{u} (\nabla \cdot \vec{\omega}) - \vec{\omega} (\nabla \cdot \vec{u}) + (\vec{\omega} \cdot \nabla) \vec{u} - (\vec{u} \cdot \nabla) \vec{\omega}$

0 0  
(div curl = 0) (continuity eqn., i.e. incompressibility condition)

$\vec{\omega}$  eqn. becomes

2/17



$$\frac{d\vec{\omega}}{dt} + (\vec{u} \cdot \nabla) \vec{\omega} = (\vec{\omega} \cdot \nabla) \vec{u} + \gamma \nabla^2 \vec{\omega}$$

$\underbrace{\hspace{10em}}$

Convective acceleration of  $\vec{\omega}$

Using total ("substantial" or "Eulerian") derivative:

$$\frac{D\vec{\omega}}{Dt} = (\vec{\omega} \cdot \nabla) \vec{u} + \gamma \nabla^2 \vec{\omega} \quad (\text{Vorticity transport eqn.})$$

"Helmholtz Vorticity eqn."

rate of change of vorticity following the fluid element  
 Change of vorticity caused by stretching or compression in the direction of the vorticity vector (also turning)

rate of diffusion of vorticity due to viscosity (analogous to the diffusion of heat)

Lugt

In tensor form:

$$\frac{\partial \omega_i}{\partial t} + u_j \frac{\partial \omega_i}{\partial x_j} = \omega_j \frac{\partial u_i}{\partial x_j} + \gamma \frac{\partial^2 \omega_i}{\partial x_j^2} \quad i=1,2,3$$

(Summation over repeated indices)

Note that in 2D flow, Stretching = 0, Vorticity transport eqn.  
 (only  $\omega_z$  is nonzero but then  $\omega_z \frac{\partial u_x}{\partial x} \equiv 0$ )  
 (becomes:)

$$\frac{D\vec{\omega}}{Dt} = \gamma \nabla^2 \vec{\omega} \quad (\text{Linear eqn.})$$

(Says that the rate of change of vorticity following a fluid element is equal to the rate of viscous diffusion)  
 (No source terms!)

The nonlinearity comes from the stretching term  $(\vec{\omega} \cdot \nabla) \vec{u}$ ,

Which is non-zero in 3-D flow.

In the absence of viscosity, we can show that vorticity moves with the fluid and increases or decreases as the fluid is stretched or compressed, respectively.

This relation can be verified immediately in Cartesian coordinates for the  $x$ -component:

$$\begin{aligned} (\vec{\omega} \cdot \nabla) u &= \omega_x \frac{\partial u}{\partial x} + \omega_y \frac{\partial u}{\partial y} + \omega_z \frac{\partial u}{\partial z}, \\ &= \omega_x \frac{\partial u}{\partial x} + \omega_y \frac{1}{2} \left( \frac{\partial v}{\partial x} + \frac{\partial u}{\partial y} \right) + \omega_z \frac{1}{2} \left( \frac{\partial w}{\partial x} + \frac{\partial u}{\partial z} \right). \end{aligned} \quad (5.11)$$

The  $y$ - and  $z$ -components are expressed correspondingly. Eq. (5.11) can be interpreted physically as the stretching and twisting of vorticity lines. The first term is in the direction of  $\omega_x$  and indicates stretching (which is a change of  $\omega_x$  itself). The other two terms represent twisting to generate  $\omega_x$ .

The appearance of the nonlinear term  $(\vec{\omega} \cdot \nabla) \vec{v}$  in the vorticity-transport equation (5.9) is unique in the sense that it does not occur in the other forms of the Navier-Stokes equations. The term  $(\vec{\omega} \cdot \nabla) \vec{v}$  is responsible for important features in vorticity dynamics that will be outlined in the course of this book. We may add that this term vanishes for two-dimensional flows since  $\vec{\omega} \cdot \nabla \equiv 0$  so that the flow features attributed to it get lost. Therefore, two-dimensional flows can present only an incomplete picture of the vorticity concept.

For general orthogonal coordinates, the components of  $(\vec{\omega} \cdot \nabla) \vec{v}$  are not as easy to obtain as those for Cartesian coordinates. Because of the importance of this term, the components of  $(\vec{\omega} \cdot \nabla) \vec{v}$  are given for both cylindrical polar coordinates and spherical polar coordinates. In cylindrical polar coordinates  $(r, \phi, z)$  they are:

$$\begin{aligned} [(\vec{\omega} \cdot \nabla) \vec{v}]_r &= \omega_r \frac{\partial v_r}{\partial r} + \omega_\phi \left( \frac{1}{r} \frac{\partial v_r}{\partial \phi} - \frac{v_\phi}{r} \right) + \omega_z \frac{\partial v_r}{\partial z}, \\ [(\vec{\omega} \cdot \nabla) \vec{v}]_\phi &= \omega_r \frac{\partial v_\phi}{\partial r} + \omega_\phi \left( \frac{1}{r} \frac{\partial v_\phi}{\partial \phi} + \frac{v_r}{r} \right) + \omega_z \frac{\partial v_\phi}{\partial z}, \\ [(\vec{\omega} \cdot \nabla) \vec{v}]_z &= \omega_r \frac{\partial v_z}{\partial r} + \omega_\phi \frac{1}{r} \frac{\partial v_z}{\partial \phi} + \omega_z \frac{\partial v_z}{\partial z}, \end{aligned} \quad (5.12)$$

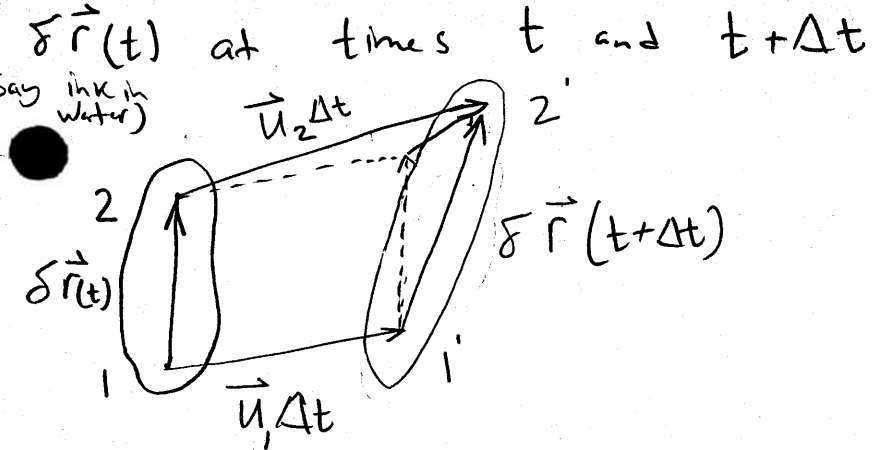
and in spherical polar coordinates  $(R, \theta, \lambda)$ :

$$\begin{aligned} [(\vec{\omega} \cdot \nabla) \vec{v}]_R &= \omega_R \frac{\partial v_R}{\partial R} + \omega_\theta \left( \frac{1}{R} \frac{\partial v_R}{\partial \theta} - \frac{v_\theta}{R} \right) + \omega_\lambda \left( \frac{1}{R \sin \theta} \frac{\partial v_R}{\partial \lambda} - \frac{v_\lambda}{R} \right), \\ [(\vec{\omega} \cdot \nabla) \vec{v}]_\theta &= \omega_R \frac{\partial v_\theta}{\partial R} + \omega_\theta \left( \frac{1}{R} \frac{\partial v_\theta}{\partial \theta} + \frac{v_R}{R} \right) + \omega_\lambda \left( \frac{1}{R \sin \theta} \frac{\partial v_\theta}{\partial \lambda} - \frac{v_\lambda}{R} \cot \theta \right), \\ [(\vec{\omega} \cdot \nabla) \vec{v}]_\lambda &= \omega_R \frac{\partial v_\lambda}{\partial R} + \omega_\theta \left( \frac{1}{R} \frac{\partial v_\lambda}{\partial \theta} \right) + \omega_\lambda \left( \frac{1}{R \sin \theta} \frac{\partial v_\lambda}{\partial \lambda} + \frac{v_R}{R} + \frac{v_\theta}{R} \cot \theta \right). \end{aligned} \quad (5.13)$$

Now it is not difficult to write the vorticity equation in those coordinates by using the corresponding parts of the Navier-Stokes equations, given in Section 3.2.

Lugt (1996)

(To prove that) Consider a blob of fluid w/ separation vector  $\vec{\delta r}(t)$  at times  $t$  and  $t+\Delta t$  3/17



$$\vec{\delta r}(t) + \vec{u}_2 \Delta t = \vec{u}_1 \Delta t + \vec{\delta r}(t+\Delta t)$$

$$\Rightarrow (\vec{u}_2 - \vec{u}_1) \Delta t = \vec{\delta r}(t+\Delta t) - \vec{\delta r}(t)$$

$$(\vec{u}_2 - \vec{u}_1) = \frac{D(\vec{\delta r})}{Dt}$$

This difference in velocity at the two end points of  $\vec{\delta r}$

can be re-written as:

$$\frac{D(\vec{\delta r})}{Dt} = (\vec{\delta r} \cdot \nabla) \vec{u} \quad \dots \dots \dots (1)$$

Variation of  $\vec{u}$  in the direction parallel to  $\vec{\delta r}$

helmholtz vorticity transport eqn. (above) in the absence of viscosity is:

$$\frac{D\vec{\omega}}{Dt} = (\vec{\omega} \cdot \nabla) \vec{u} \quad \dots \dots \dots (2)$$

If we multiply (1) by an arbitrary constant K and subtract (2) from it, get:

$$\frac{D}{Dt} (K \vec{\delta r} - \vec{\omega}) = [(K \vec{\delta r} - \vec{\omega}) \cdot \nabla] \vec{u}$$

(Implications of this:)

Suppose at  $t=0$  choose  $K$  such that  $K \vec{\delta r} = \vec{\omega}$

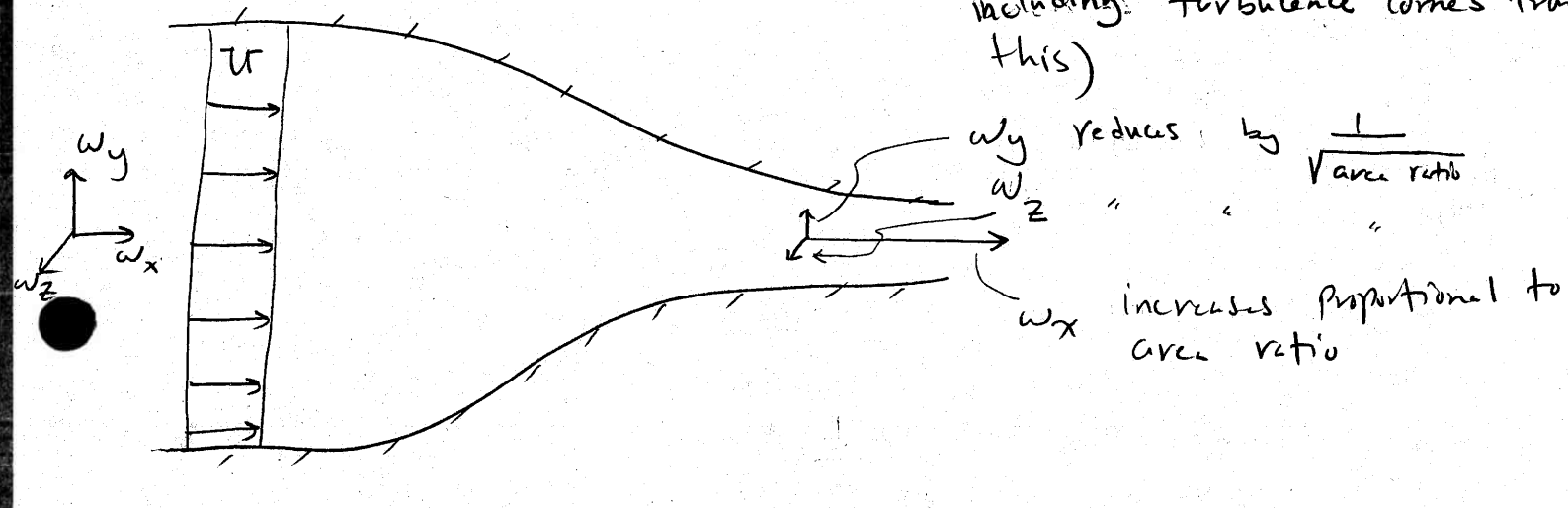
i.e. mark the fluid so that  $K \vec{\delta r}$  is equal in magnitude and direction to vorticity,

then for all time  $t > 0$   $K \vec{\delta r} = \vec{\omega}$  Means Physically that vorticity moves w/ fluid

Thus

$$\frac{D\vec{\omega}}{Dt} = (\vec{\omega} \cdot \nabla) \vec{u} + \gamma \nabla^2 \vec{\omega}$$

↑ Stretching term (and the nonlinearity of 3D flow including turbulence comes from this)



Consider the non-dimensional form of vorticity eqn.

(Assuming that flow characteristic length & Velocity are:)

$L$  and  $U$  (dimensionless)

Define  $\vec{\omega}^* = \frac{\vec{\omega}}{U L}$  ( $\text{since } |w| = \frac{1}{t}$ )

$$t^* = \frac{t U}{L}, \quad \vec{x}^* = \frac{\vec{x}}{L}, \quad \vec{u}^* = \frac{\vec{u}}{U}, \quad \nabla^* = L \nabla$$

Vorticity eqn. becomes:

$$\frac{D\vec{\omega}^*}{Dt^*} = (\vec{\omega}^* \cdot \nabla^*) \vec{u}^* + \frac{1}{Re} \nabla^{*2} \vec{\omega}^*$$

Observe that if  $Re \ll 1$ , stretching not important (because vorticity diffuses out of fluid element before it has stretched). If  $Re \gg 1$ , the stretching controls flow except near wall where  $\vec{u} = 0$ .

(All of analysis above has been for incompressible flow)

on vorticity transport eqn.

(to see the effect of compressibility, it suffices to start w/ the Euler eqn. (i.e. since we have already looked at the effect of viscosity, we don't need the N-S eqn.)

$$\frac{\partial \vec{u}}{\partial t} + \nabla \left( \frac{1}{2} \vec{u}^2 \right) - \vec{u} \times \vec{\omega} = -\frac{1}{\rho} \nabla p \quad (+ \gamma \nabla^2 \vec{\omega})$$

take curl and rewrite:

$$(\text{curl } f \vec{B} = f \text{curl } \vec{B} + \text{grad } f \times \vec{B})$$

$$\frac{D \vec{\omega}}{Dt} = (\vec{\omega} \cdot \nabla) \vec{u} - \vec{\omega} \text{div } \vec{u} + \underbrace{(\nabla p \times \nabla \left( \frac{1}{\rho} \right))}_{-\frac{1}{\rho} \text{curl } \nabla p + \nabla \left( -\frac{1}{\rho} \right) \times \nabla p}$$

(as before)

if  $\rho = \text{const}$ ,  $D \frac{1}{\rho} = 0$  then  $\nabla p \times \nabla \frac{1}{\rho} = 0$  (and  $\text{div } \vec{u} = 0$  recover earlier result)

also,

if  $\rho = \rho(p)$  "barotropic" state then  $\nabla p \times \nabla \frac{1}{\rho} = 0$

If  $\rho \neq \rho(p)$  (e.g.  $\rho = \rho(p, T)$ ) "baroclinic" state,  
and the vorticity generation from this term is called baroclinic vorticity

(Since  $\nabla p$  and  $\nabla \rho$  are not necessarily parallel, pressure forces can exert a torque on fluid element, thus changing its angular momentum)  $\nabla p \rightarrow \begin{matrix} \text{---} \\ \text{---} \end{matrix} \downarrow \nabla \rho$

(this is the mechanism that, for example, produces vorticity in a

Curved shock, (more about vorticity generation a little later)  
(end of  $\rho \neq \text{const.}$ )

Transport Eqn. for Circulation,  $\Gamma = \oint \vec{u} \cdot d\vec{l}$

T.P. T.P. T.P.

## 6.6 CROCCO'S THEOREM: A RELATION BETWEEN THE THERMODYNAMICS AND FLUID KINEMATICS OF A COMPRESSIBLE FLOW

Consider again an element of fluid as it moves through a flowfield. The movement of this fluid element is both translational and rotational. The translational motion is denoted by the velocity  $\mathbf{V}$ . The rotational motion is denoted by the angular velocity,  $\boldsymbol{\omega}$ . In any basic fluid mechanic text, it is readily shown that  $\boldsymbol{\omega} = \frac{1}{2}\nabla \times \mathbf{V}$ ; hence the curl of the velocity field at any point is a measure of the rotation of a fluid element at that point. The quantity  $\nabla \times \mathbf{V}$  is itself denoted as the *vorticity* of the fluid; the vorticity is equal to twice the angular velocity.

In this section, we will derive a relationship between the fluid vorticity (a kinematic property of the flow) and the pertinent thermodynamic properties. To begin, consider Euler's equation, Eq. (6.29), without body forces,

$$\rho \frac{D\mathbf{V}}{Dt} = -\nabla p \quad (6.53)$$

Writing out the substantial derivative, Eq. (6.53) is

$$\rho \frac{\partial \mathbf{V}}{\partial t} + \rho(\mathbf{V} \cdot \nabla)\mathbf{V} = -\nabla p \quad (6.54)$$

Recall the combined first and second laws of thermodynamics in the form of Eq. (1.32). In terms of changes in three-dimensional space, the differentials in Eq. (1.32) can be replaced by the gradient operator,

$$T\nabla s = \nabla h - v\nabla p = \nabla h - \frac{\nabla p}{\rho} \quad (6.55)$$

Combining Eqs. (6.54) and (6.55),

$$T\nabla s = \nabla h - \frac{1}{\rho} \left[ -\rho \frac{\partial \mathbf{V}}{\partial t} - \rho(\mathbf{V} \cdot \nabla)\mathbf{V} \right]$$

$$\text{or} \quad T\nabla s = \nabla h + \frac{\partial \mathbf{V}}{\partial t} + (\mathbf{V} \cdot \nabla)\mathbf{V} \quad (6.56)$$

However, from the definition of total enthalpy,

$$h \equiv h_o - \frac{V^2}{2}$$

$$\text{Hence} \quad \nabla h = \nabla h_o - \nabla \left( \frac{V^2}{2} \right) \quad (6.57)$$

Substitute Eq. (6.57) into (6.56):

$$T\nabla s = \nabla h_o - \nabla \left( \frac{V^2}{2} \right) + \frac{\partial \mathbf{V}}{\partial t} + (\mathbf{V} \cdot \nabla)\mathbf{V} \quad (6.58)$$

(From Anderson, Modern Compressible Flow)

Using the vector identity

$$\nabla \left( \frac{V^2}{2} \right) - (\mathbf{V} \cdot \nabla) \mathbf{V} = \mathbf{V} \times (\nabla \times \mathbf{V})$$

Eq. (6.58) becomes

$$T \nabla s = \nabla h_o - \mathbf{V} \times (\nabla \times \mathbf{V}) + \frac{\partial \mathbf{V}}{\partial t}$$

(6.59)

Equation (6.59) is called *Crocco's theorem*, because it was first obtained by L. Crocco in 1937 in a paper entitled "Eine neue Stromfunktion fur die Erforschung der Bewegung der Gase mit Rotation," *Z. Angew. Math. Mech.* vol. 17, 1937, pp. 1-7.

For steady flow, Crocco's theorem becomes

$$T \nabla s = \nabla h_o - \mathbf{V} \times (\nabla \times \mathbf{V})$$

(6.60)

Keep in mind that Eqs. (6.59) and (6.60) hold for an inviscid flow with no body forces.

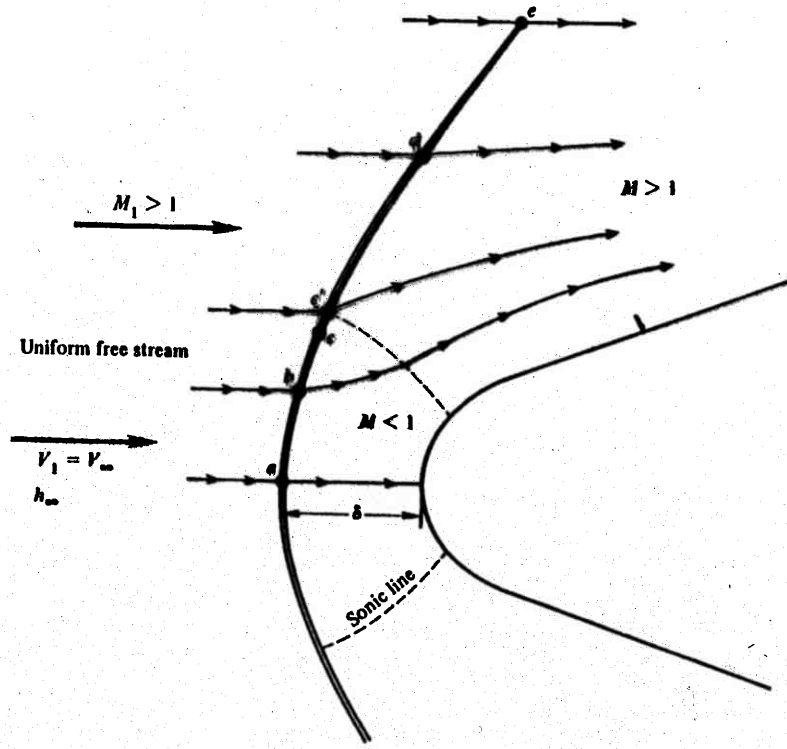
Rearranging Eq. (6.60),

$$\mathbf{V} \times (\nabla \times \mathbf{V}) = \underbrace{\nabla h_o}_{\text{vorticity}} - \underbrace{\frac{-T \nabla s}{\text{gradient of entropy}}}_{\text{total enthalpy gradient}}$$
(6.61)

Equation (6.61) has an important physical interpretation. When a steady flowfield has gradients of total enthalpy and/or entropy, Eq. (6.61) dramatically shows that it is *rotational*. This has definite practical consequences in the flow behind a curved shock wave, as sketched in Fig. 4.23. In region 1 ahead of the curved shock, all streamlines in the uniform free stream have the same total enthalpy,  $h_{o_1} = h_\infty + V_\infty^2/2$ . Across the stationary shock wave, the total enthalpy does not change; hence, in region 2 behind the shock,  $h_{o_2} = h_{o_1}$ . Hence, all streamlines in the flow behind the shock have the same total enthalpy; thus, behind the shock,  $\nabla h_o = 0$ . However, in Fig. 4.23 streamline (b) goes through a strong portion of the curved shock and hence experiences a higher entropy increase than streamline (d), which crosses a weaker portion of the shock. Therefore, in region 2,  $\nabla s \neq 0$ . Consequently, from Crocco's theorem as given in Eq. (6.61),  $\mathbf{V} \times (\nabla \times \mathbf{V}) \neq 0$  behind the shock. Thus,

$$\nabla \times \mathbf{V} \neq 0 \quad \text{behind the shock}$$

Hence, Crocco's theorem shows that the *flowfield behind a curved shock is rotational*. This is unfortunate, because rotational flowfields are inherently more



$$\frac{D\Gamma}{Dt} = \oint \underbrace{\frac{D\vec{U}}{Dt} \cdot d\vec{l}}_{\downarrow \text{momentum Eqn.}} + \oint \vec{U} \cdot d\left(\frac{D\vec{l}}{Dt}\right)$$

(Transport eqn for  $\Gamma$ :)  $\Gamma' \equiv \oint \vec{U} \cdot d\vec{l}$

$$= \oint -\frac{\nabla P}{\rho} \cdot d\vec{l} + \oint \vec{U} \cdot d(\vec{U})$$

For inviscid flow

$$= 0 \quad \begin{matrix} \downarrow \\ \text{if } \rho = \rho(P) \\ (\text{like the definition of a thermodynamic state}) \end{matrix} + \oint \frac{d|\vec{U}|^2}{2} = 0$$

for  $\rho = \rho(P)$  (or constant), circulation around a material curve is independent of time

$$\boxed{\frac{D\Gamma}{Dt} = 0}$$

"Kelvin's Circulation Theorem"

(for inviscid flow)

Initial and Boundary Conditions

(eqn. of motion for an incompressible flow)  
(Cont. & N-S eqns.)

(While we have extensively discussed the N-S eqn. and its counterpart, the Vorticity transport eqn. We haven't yet given detailed analysis of the BCs for Velocity and Vorticity)

$$\operatorname{div} \vec{U} = 0 \quad \dots \quad (1)$$

$$\frac{\partial \vec{U}}{\partial t} + (\vec{U} \cdot \nabla) \vec{U} = -\frac{1}{\rho} \nabla P + \gamma D^2 \vec{U} \quad \dots \quad (2)$$

(noting)  
"Primitive-Variable formulation" of Navier-Stokes

In principle, an initial-boundary value problem is completely defined if we prescribe initial and boundary conditions.

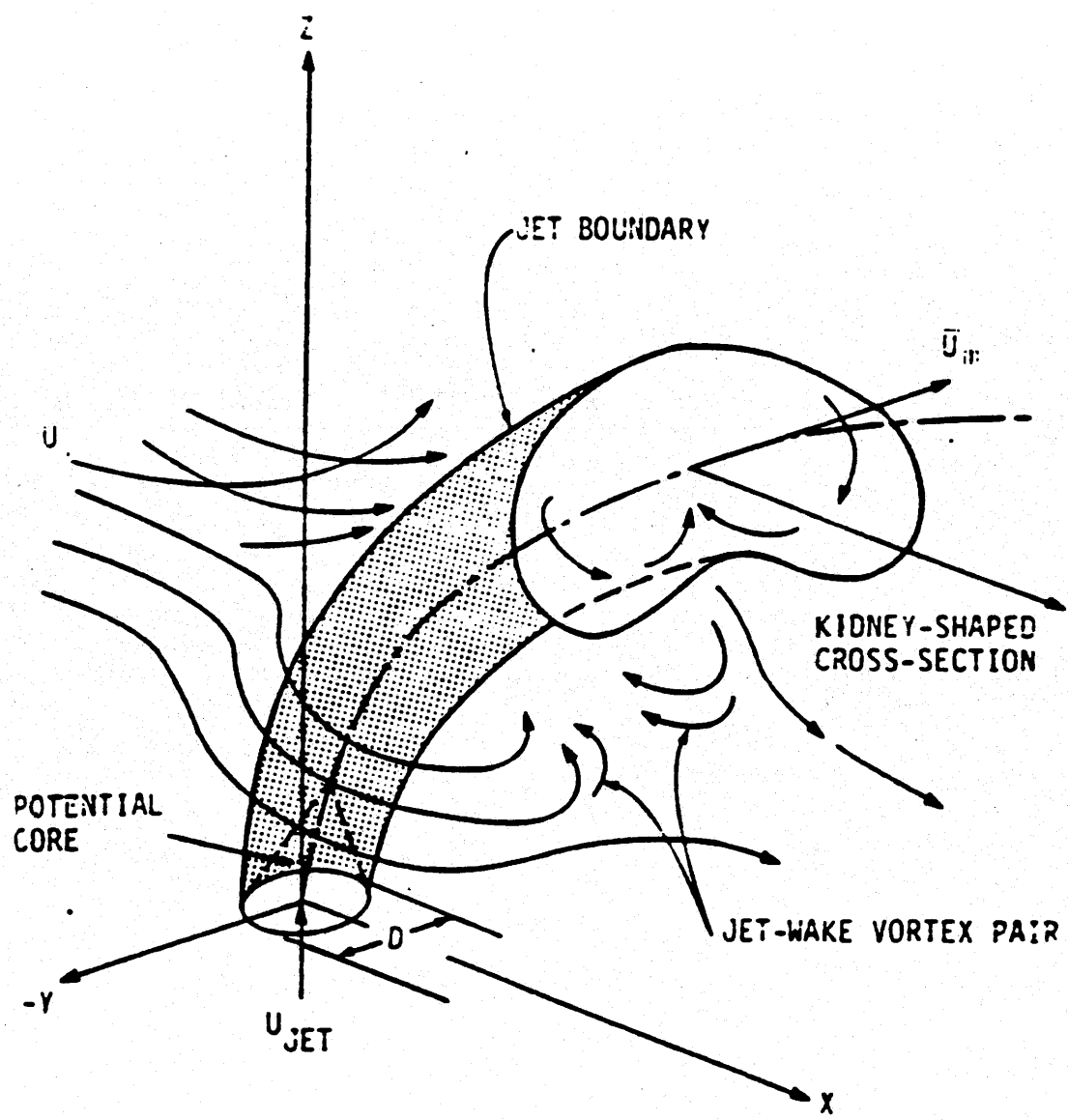


**Fig. 1 The round turbulent jet in a crossflow**

- A Very Useful Paper

- Excellent approach to the problem

## STRUCTURE IN THE NEAR FIELD OF THE TRANSVERSE JET

T.F. Fric and A. Roshko

Graduate Aeronautical Laboratories  
California Institute of Technology  
Pasadena, CA 91125

### ABSTRACT

Photographs of a jet issuing from a wall into a crossflow display the four types of vortical structures which exist in the near field: namely, the jet shear layer vortices, the nascent far field vortex pair, the near wall horseshoe vortices, and a system of vortices in the wake of the jet. It is shown that the wake vorticity is not "shed" from the jet but is formed from vorticity which originated in the wall boundary layer. The sources of vorticity for the other types of structures are also briefly discussed.

### NOMENCLATURE

$D_c$	circular cylinder diameter
$D_j$	jet diameter
$f_{sep}$	crossflow boundary layer separation power
$f_w$	spectral peak frequency
$Re_{cf}$	wake power spectral peak frequency
$Re_j$	nominal* crossflow Reynolds number
$St_{sep}$	$= U_{cf} D_j / \nu$ or $U_{cf} D_c / \nu$
$St_w$	nominal* jet Reynolds number = $VR Re_{cf}$
$U_{cf}$	crossflow boundary layer separation Strouhal number = $f_{sep} D_j / U_{cf}$
$VR$	wake Strouhal number = $f_w D_j / U_{cf}$
$X, Y, Z$	nominal* crossflow velocity
$\delta_{cf}$	nominal* jet to crossflow velocity ratio
$\delta_j$	crossflow, lateral, and jet directions, respectively
	nominal* crossflow boundary layer displacement thickness at $X/D_j = 0$
	nominal* jet axisymmetric shear layer displacement thickness at $Z/D_j = 0$
	* nominal refers to values measured with either no crossflow or no jet, as appropriate.

### 1. INTRODUCTION

Jet injection is used widely in many technical applications, often to mix the injected fluid with that of the crossflow into which it is injected. Our interest in the experiments reported here is in the physics and structure of turbulent entrainment and mixing in the near field of the incompressible transverse jet. The near field is defined somewhat arbitrarily to include the first few jet diameters of the flow, where most of the jet's bending occurs and where the crossflow/jet interaction dynamics is the most complex.

There have been numerous prior investigations of both the near and far fields of the transverse jet. Experimental, analytical, and computational work in the far field has concentrated on either the measuring of (e.g. Fearn & Weston 1974) or the modelling of (e.g. Broadwell & Breidenthal 1984, Karagozian & Greber 1984) the counterrotating pair of vortices, which comprises the transverse jet's far field. The near field has also received considerable attention (e.g. McMahon, Hester & Palfrey 1971; Moussa, Trischka & Eskinazi 1977; Foss 1980). Although many observations have been made, and models have been constructed, there is still no complete understanding of the structure in the near field of the transverse jet.

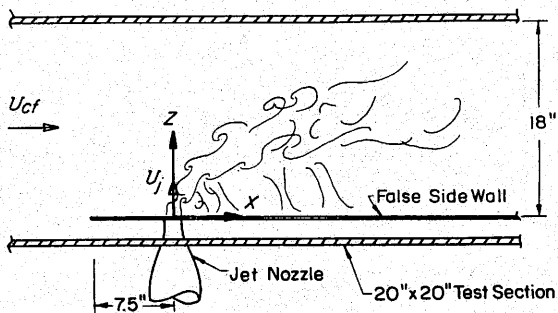


FIGURE 1: Experimental set-up.

The experiments were performed in GALCIT's 20" by 20" open-return low speed wind tunnel. Figure 1 shows the experimental set-up. To afford better control of the boundary layer on the wall from which the jet issues, a false side wall was used. In this paper, the false side wall is referred to as the crossflow wall, and the boundary layer on this wall as the crossflow boundary layer. The rms turbulence level of the crossflow was about .2%. The jet, supplied by a 1.5" diameter nozzle had a nearly top hat velocity profile. The nozzle was mounted flush with the crossflow wall. The jet was supplied by a centrifugal blower; jet turbulence intensity levels of .5% to 1% were achieved with the appropriate use of flow management upstream of the nozzle. Flow conditions of  $2 \leq VR \leq 10$

$Re_x = \text{Reynolds number based on distance to L.E. of false wall}$

$19,000 \leq Re_x \leq 57,000$

and  $3800 \leq Re_{cf} \leq 11400$  (correspondingly,  $7600 \leq Re_j \leq 114,000$ ) were investigated.

## 2. THE DOMINANT NEAR FIELD VORTICAL STRUCTURES

The dominant vortical structures observed in the transverse jet's near field are the following:

- (a) Distorted shear layer ring vortices at the circumference of the bending jet.
- (b) The inception of the counterrotating pair of vortices which eventually dominates the far field jet structure.
- (c) A system of horseshoe or collar vortices at the crossflow wall.
- (d) A system of wake vortices nearly aligned with the initial jet direction.

The smoke-wire flow visualization technique (Corke *et al.* 1977) with strobe lighting was used (except where noted). Examples of each of these structures are shown in the figures which follow.

Figure 2 shows the bending jet's distorted ring vortices. The approaching streaklines, visualized with a smoke-wire upstream in the XZ plane, are entrained into the leading edge shear layer of the jet. As a result of axial flow along the cores of the distorted vortex rings, the smoke is seen coming out of that plane. In this case,  $\delta_j/D_j \approx .03$ . Such a shear layer roll-up is analogous to what is observed in a free jet. Features similar to these ring vortices are seen over the range of  $VR$  and  $Re_{cf}$  studied here.

Results indicate that the counterrotating pair of vortices, which is universally considered to dominate the mean far field structure of the jet, begins forming quite early. For example, figure 3 shows a nearly planar slice of the flow at  $X/D_j = 1$ . Smoke begins in the crossflow boundary layer, is entrained away from the wall at the lee side of the jet, and then visualizes a structure which suggests a counterrotating vortex pair. Such a structure is observed for the complete range of  $VR$  and  $Re_{cf}$ .

Due to the adverse pressure gradient just ahead of the jet on the crossflow wall, the approaching laminar boundary layer separates and forms a system of horseshoe vortices. In figure 4, smoke begins in the crossflow boundary layer. Here  $\delta_{cf}/D_j \approx .06$ . The near wall flow around a wall-mounted circular cylinder also forms such structures. The upstream portions of the horseshoe vortices are visually similar for all  $VR$  and  $Re_{cf}$ , but such is not the case for the downstream portions (legs) of these structures. For  $X/D_j \gtrsim 0$ , the near wake, whose structure strongly depends on  $VR$ , affects the dynamics of the horseshoes' legs. In figure 2, cross sections of two horseshoe vortices are faintly visible just upstream of the jet.

Possibly the most intriguing and least understood of the structures in the near field are the wake vortices. Figure 5 shows a side view of the wake structures, while in figure 6 one sees a nearly cross sectional view. Kuzo & Roshko (1984) have observed that such wake structures persist

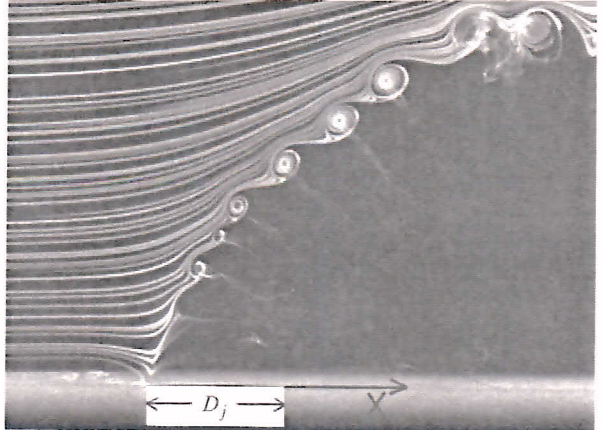


FIGURE 2: Jet's distorted ring vortices. In this case, the vortices tilt clockwise. The jet issues from the bottom, as indicated, and the crossflow is from left to right.  $VR = 2$ ,  $Re_{cf} = 3800$ .

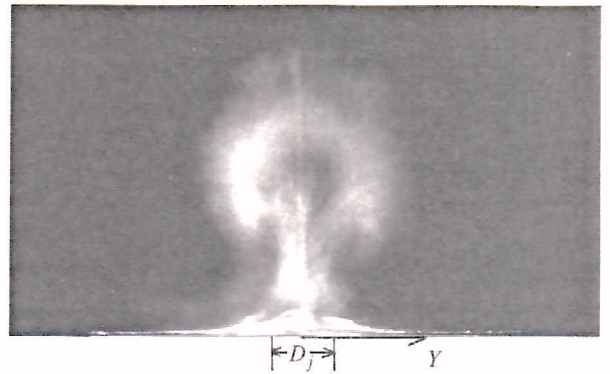


FIGURE 3: Early indication of the counterrotating vortex pair. Looking upstream, a vertical "sheet" of light is at  $X/D_j = 1$ .  $VR = 4$ ,  $Re_{cf} = 3800$ .

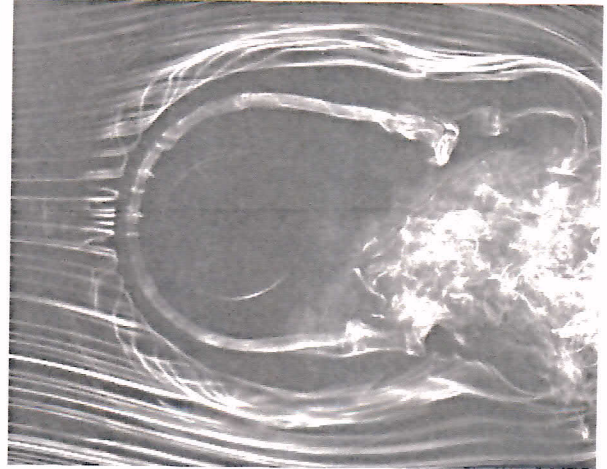


FIGURE 4: Horseshoe vortex system. The jet, near the center of the photograph, issues directly at the viewer.  $VR = 2$ ,  $Re_{cf} = 3800$ .

several hundred jet diameters downstream. A wake exists for all  $VR$  and  $Re_{cf}$  studied, but its regularity and qualitative appearance varies with  $VR$  and  $Re_{cf}$ .

The structures displayed in our photographs have been either directly observed or indirectly inferred previously in the literature (*cf.* references mentioned previously or elsewhere in this paper and also their reference lists). The dynamics of the structures' formation, however, has not been consistently explained, at least not in terms of the constraints imposed by vorticity generation mechanisms.

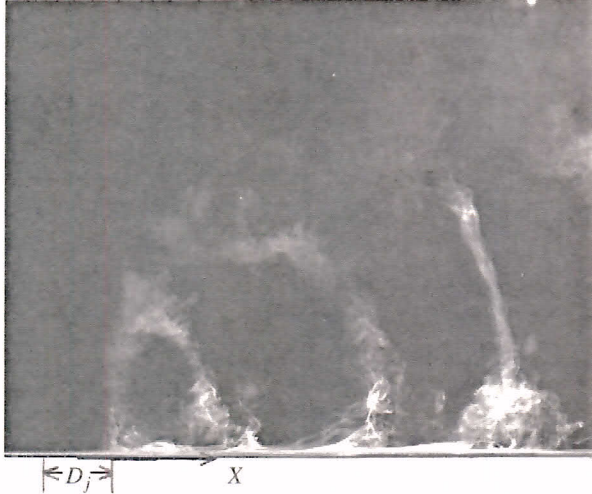


FIGURE 5: Wake vortices in side view. The smoke is initially in the crossflow boundary layer.  $VR = 4$ ,  $Re_{cf} = 3800$ .

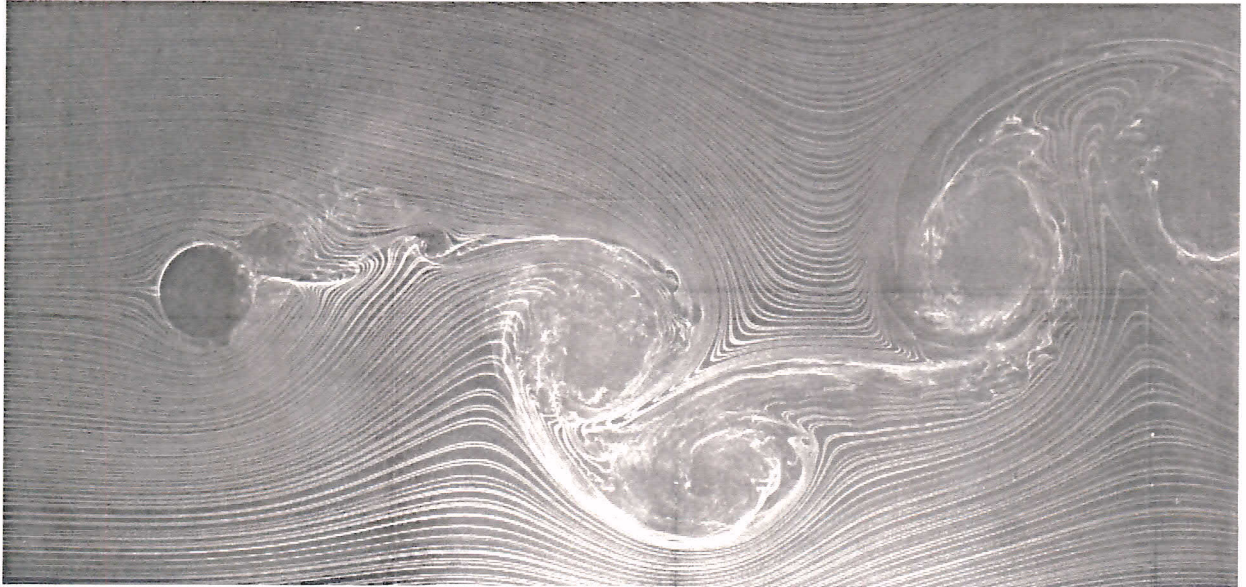


FIGURE 6: Wake vortices in cross section. The jet, near the left side of the photograph, issues directly at the viewer. The smoke-wire is at  $Z/D_j = .5$ .  $VR = 4$ ,  $Re_{cf} = 11400$ .

### 3. SOURCES OF VORTICITY AND STRUCTURE FORMATION

Since the near field is dominated by several distinct types of vortical structures, it is of interest to try to understand their origin and formation. In particular, the source and subsequent dynamics of the vorticity leading to the structures presented in §2 are described here.

The vorticity equation for a Newtonian, barotropic, and incompressible flow with no body forces is given by

$$\frac{D\omega}{Dt} = \omega \cdot \nabla u + v \nabla^2 \omega , \quad (1)$$

where  $\omega = \nabla \times u$  is the vorticity. As is emphasized by Morton (1984), eqn. (1) does not explicitly contain any vorticity generation terms; it shows only that vorticity is convected, stretched, turned, and diffused. New vorticity can only enter a flow through imposed initial conditions and/or wall boundary conditions; there are no sources of new vorticity within the flow. This is a fundamental point when considering the formation of the wake structures in particular, as will be seen presently.

Defining the vorticity flux out of a wall as  $\hat{n} \tilde{J}_0$ , where  $\tilde{J}_0 = -v(\nabla \omega)_0$  is the vorticity flux tensor at the wall and  $\hat{n}$  is the wall-normal unit vector, it can be shown (Wu, Wu & Wu 1987) that for nonaccelerating and nonrotating surfaces

$$\rho \hat{n} \cdot \tilde{J}_0 = -\hat{n} \times (\nabla p)_0 - \hat{n} [\hat{n} \cdot (\nabla \times \tau_0)] + (\hat{n} \times \tau_0) \cdot \nabla \hat{n} . \quad (2)$$

The first term on the right-hand side of eqn. (2) represents the vorticity source term due to a wall pressure gradient. The second term accounts for the gradient of wall-normal vorticity due to a wall shear stress  $\tau_0$  with a nonzero  $\nabla \times \tau_0$  wall-normal component. Finally, the third term accounts for the effects of wall curvature transverse to the wall shear

stress direction. With the above discussion in mind, the sources of vorticity for the four kinds of structures mentioned in §2 can be identified.

The source of the distorted ring vorticity of the jet is the boundary layer vorticity in the nozzle supplying the jet flow, again directly analogous to a free jet. The initial nearly axisymmetric shear layer leaving the jet becomes unstable and forms the ring-like vortices.

We believe that the counterrotating vortex pair evolves from the shear layer vorticity of the jet, *i.e.* its ultimate source is in the vorticity issuing from the nozzle. In fact, the numerical results of Coehlo & Hunt (1989) suggest that this process has already begun within the boundary layer of the nozzle; the effects of the crossflow are felt within the nozzle. From numerical results, Sykes, Lewellen & Parker (1986) have previously suggested that the jet's ring vorticity may evolve into the counterrotating pair.

The source of vorticity for the horseshoe structures is in the approaching crossflow boundary layer and the crossflow wall region near the jet. The separated crossflow boundary layer ahead of the jet supplies the horseshoes with vorticity, and in addition the horseshoe vortices induce pressure gradients on the wall, thereby generating more vorticity.

That no new vorticity can be generated within the flow is essential to the proper description of the wake formation. To our knowledge, in every paper in which the transverse jet's wake formation has been discussed previously, the wake vorticity has been described as vorticity "shed" from the jet and/or as vorticity due to a jet/crossflow interaction analogous to a solid cylinder/crossflow interaction. Since the jet does not offer the crossflow a solid surface on which to generate new vorticity, as a solid cylinder does, such analogies are physically wrong and lead to an incorrect explanation of the wake formation. As will be addressed in §4, the actual events leading to the appearance of vortices in the wake of the jet appear to be quite different and more complex.

#### 4. WAKE CHARACTERISTICS AND WAKE FORMATION MODEL

This section is devoted to the vortical structures in the jet's wake. The wake is especially interesting because, even though it is qualitatively similar in appearance to a circular cylinder wake, its formation must be very different. The vorticity which is shed from a solid cylinder is vorticity which was generated solely at the surface of the cylinder; the pressure gradient production term in eqn. (2) is responsible. There is no such mechanism in the present case of a flow around a jet, since there is *no* no-slip condition at the jet/crossflow interface. The vorticity in the jet's wake must be vorticity which originated at a solid boundary, either within the nozzle or at the crossflow wall.

To study the wake further, smoke from different sources was used to track fluid. Smoke is considered to be a suitable marker of vorticity for our purposes. Since the effective Schmidt number for smoke is large, vorticity

diffuses faster than smoke does; we assume that once the vorticity is tagged, the smoke marks the cores of vortices. In figure 7, the jet is tagged by seeding the jet supply with cigarette smoke. A well-defined jet body is seen with no presence of smoke nor, apparently, jet fluid in the wake. Conversely, when the crossflow boundary layer is tagged with smoke, as was seen in figure 5, most of the smoke ends up in the wake vortices. These results suggest that the jet vorticity does not contribute to the wake vorticity. Not only does the jet not act like a solid cylinder, not generating any new vorticity, it also does not shed any of its vorticity to the wake. Rather, the source of the wake vorticity is the crossflow boundary layer.

It is clearly of interest to determine whether the wake vortices convect with a characteristic (**Strouhal**) frequency. Accordingly, frequency measurements were made using a hot-wire anemometer placed in the wake of the jet. The values, shown in figure 8, are independent of the hot-wire's location in the wake. These values of  $St_w$  are based on the rms average of 32 individual power spectra, obtained with an HP 3582A spectrum analyzer. In general, the spectral peaks  $f_w$  (dominant frequencies) are not as sharply defined here as they would be in the wake of a solid cylinder, and the values of  $St_w$  are somewhat lower than they are for a circular cylinder wake at the same  $Re_{cf}$ . The sharpness of the spectral peaks varies considerably with  $VR$ , but for each  $Re_{cf}$  investigated, the sharpest peaks were recorded for  $3.5 \leq VR \leq 4.5$ . This is also the range of  $VR$  for which the values of  $St_w$  appear to be independent of  $Re_{cf}$ . Our values of  $St_w$  are in the same range as those measured by Moussa *et al.* (1977).

For the purpose of verifying the source of the wake vorticity, spectra were also taken near the region denoted by the arrows in figure 9, where smoke is tagging the crossflow



FIGURE 7: The jet, issuing from the bottom left-hand portion of the photograph, is tagged with smoke. This view is the same as in figure 5.  $VR = 4$ ,  $Re_{cf} = 3800$ .

boundary layer fluid. Upstream of the jet, a portion of the crossflow boundary layer separates and forms a horseshoe vortex. The boundary layer fluid outside the horseshoe structures on the jet's  $+Y$  side wraps around the jet and then separates on the its lee side, near the arrows in figure 9. The previous separation event, on the  $-Y$  side of the jet, has convected further downstream. Figure 10 shows the values for  $St_{sep}$  measured near such separation events; the agreement with Strouhal numbers measured in the wake is very good. Also, the sharpest spectral peaks are again seen for  $3.5 \leq VR \leq 4.5$ . These results support our conclusion that the source of the wake vorticity is in the crossflow boundary layer; that the characteristic frequencies of the separation events match those of the wake structures implies a connection between the two. The crossflow boundary layer separating at the downstream side of the jet to subsequently feed the wake is consistent with figure 5, where smoke seeding the crossflow boundary layer leaves

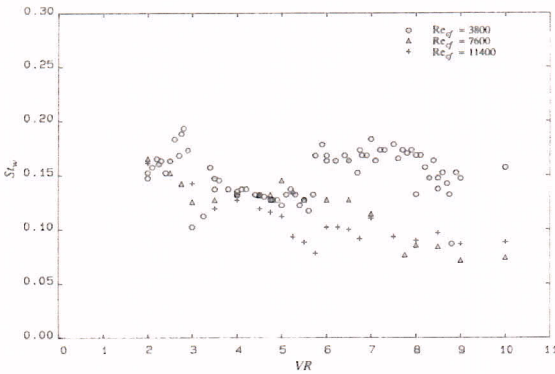


FIGURE 8: Wake Strouhal number dependence on velocity ratio at  $Re_{cf} = 3800$  ( $\circ$ ), 7600 ( $\Delta$ ) and 11400 ( $+$ ). Measured at  $X/D_j = 3.5$ ,  $Y/D_j = 1.5$ ,  $Z/D_j = .5$ .

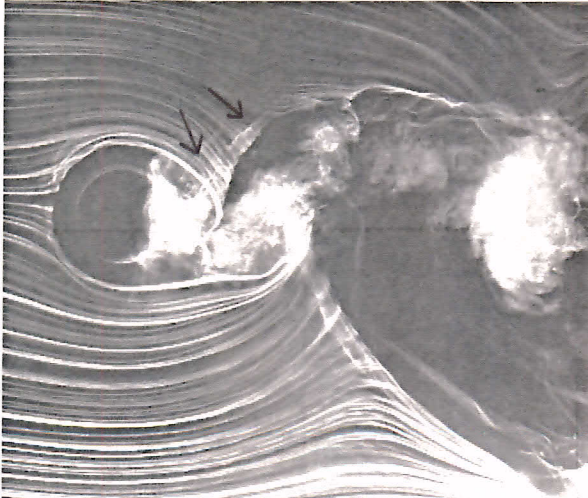


FIGURE 9: Separation event. A separation of the crossflow boundary layer is indicated by the arrows.  $VR = 4$ ,  $Re_{cf} = 3800$ .

the wall aft of the jet. We conclude that the crossflow boundary layer separation events represent the inception of the transverse jet's wake formation.

A striking difference between the wake of a cylinder and jet is evident when comparing figure 11 with 6. In both cases, the smoke-wire is located at  $Z/D_j = .5$  (or, equivalently,  $Z/D_c = .5$ ) and  $Re_{cf} = 11400$ . The flow around the jet in figure 6 looks nearly potential; the near wake streaklines are closed. Conversely, the flow around the cylinder separates, thereby opening the near wake. The potential-like streakline pattern around the jet has important implications for the crossflow boundary layer flow; the adverse pressure gradient on the lee side of the jet is imposed on the crossflow wall. This adverse pressure

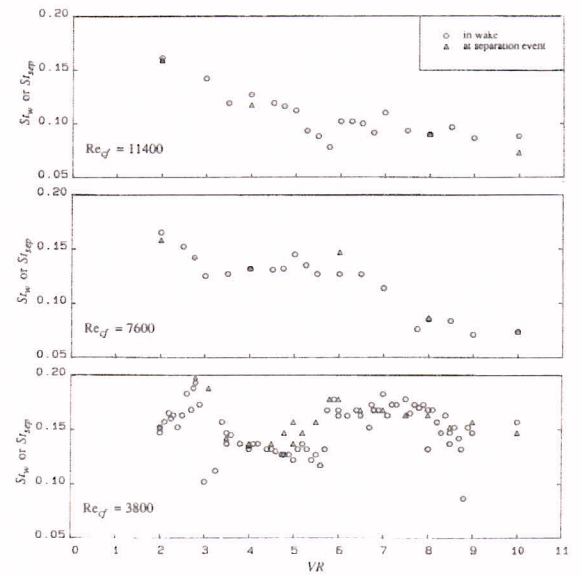


FIGURE 10: Comparison of wake ( $\circ$ ) and separation events' ( $\Delta$ ) Strouhal numbers.  $St_{sep}$  measured near the cross-flow boundary layer separation events.  $St_w$  measured at  $X/D_j = 3.5$ ,  $Y/D_j = 1.5$ ,  $Z/D_j = .5$ .

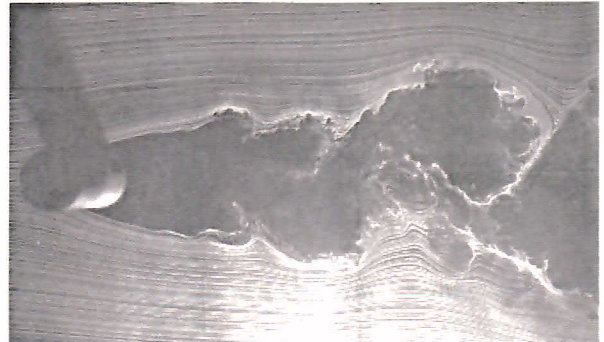


FIGURE 11: Circular cylinder wake in cross section. The cylinder is at the left end of the photograph. The aspect ratio of the wall-mounted cylinder is 6.  $Re_{cf} = 11400$ .

and  $3800 \leq Re_{cf} \leq 11400$  (correspondingly,  $7600 \leq Re_j \leq 114,000$ ) were investigated.

## 2. THE DOMINANT NEAR FIELD VORTICAL STRUCTURES

The dominant vortical structures observed in the transverse jet's near field are the following:

- (a) Distorted shear layer ring vortices at the circumference of the bending jet.
- (b) The inception of the counterrotating pair of vortices which eventually dominates the far field jet structure.
- (c) A system of horseshoe or collar vortices at the crossflow wall.
- (d) A system of wake vortices nearly aligned with the initial jet direction.

The smoke-wire flow visualization technique (Corke *et al.* 1977) with strobe lighting was used (except where noted). Examples of each of these structures are shown in the figures which follow.

Figure 2 shows the bending jet's distorted ring vortices. The approaching streaklines, visualized with a smoke-wire upstream in the  $XZ$  plane, are entrained into the leading edge shear layer of the jet. As a result of axial flow along the cores of the distorted vortex rings, the smoke is seen coming out of that plane. In this case,  $\delta_j/D_j \approx .03$ . Such a shear layer roll-up is analogous to what is observed in a free jet. Features similar to these ring vortices are seen over the range of  $VR$  and  $Re_{cf}$  studied here.

Results indicate that the counterrotating pair of vortices, which is universally considered to dominate the mean far field structure of the jet, begins forming quite early. For example, figure 3 shows a nearly planar slice of the flow at  $X/D_j = 1$ . Smoke begins in the crossflow boundary layer, is entrained away from the wall at the lee side of the jet, and then visualizes a structure which suggests a counterrotating vortex pair. Such a structure is observed for the complete range of  $VR$  and  $Re_{cf}$ .

Due to the adverse pressure gradient just ahead of the jet on the crossflow wall, the approaching laminar boundary layer separates and forms a system of horseshoe vortices. In figure 4, smoke begins in the crossflow boundary layer. Here  $\delta_{cf}/D_j \approx .06$ . The near wall flow around a wall-mounted circular cylinder also forms such structures. The upstream portions of the horseshoe vortices are visually similar for all  $VR$  and  $Re_{cf}$ , but such is not the case for the downstream portions (legs) of these structures. For  $X/D_j \geq 0$ , the near wake, whose structure strongly depends on  $VR$ , affects the dynamics of the horseshoes' legs. In figure 2, cross sections of two horseshoe vortices are faintly visible just upstream of the jet.

Possibly the most intriguing and least understood of the structures in the near field are the wake vortices. Figure 5 shows a side view of the wake structures, while in figure 6 one sees a nearly cross sectional view. Kuzo & Roshko (1984) have observed that such wake structures persist

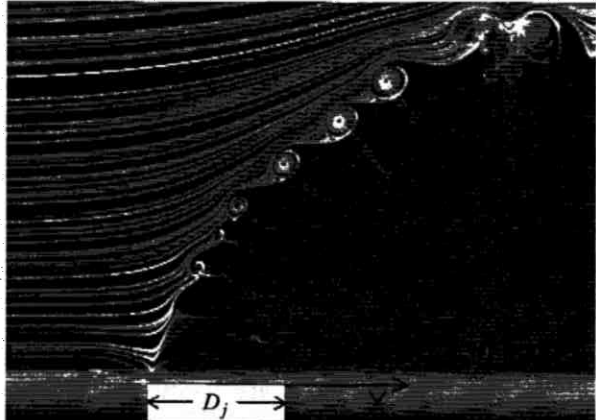


FIGURE 2: Jet's distorted ring vortices. In this case, the vortices tilt clockwise. The jet issues from the bottom, as indicated, and the crossflow is from left to right.  $VR = 2$ ,  $Re_{cf} = 3800$ .

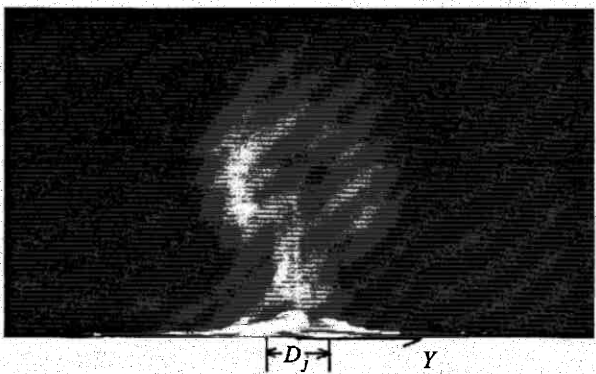


FIGURE 3: Early indication of the counterrotating vortex pair. Looking upstream, a vertical "sheet" of light is at  $X/D_j = 1$ .  $VR = 4$ ,  $Re_{cf} = 3800$ .

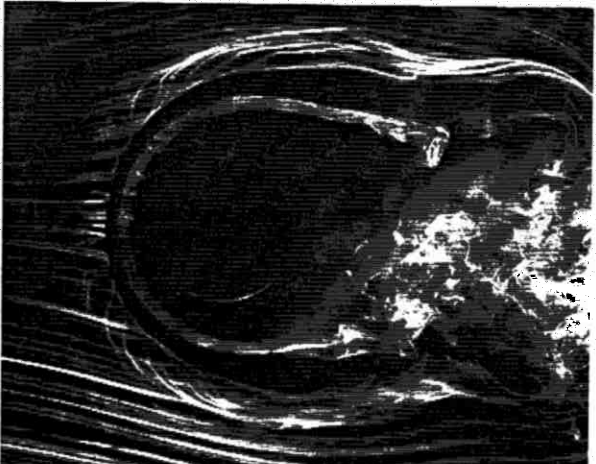


FIGURE 4: Horseshoe vortex system. The jet, near the center of the photograph, issues directly at the viewer.  $VR = 2$ ,  $Re_{cf} = 3800$ .

several hundred jet diameters downstream. A wake exists for all  $VR$  and  $Re_{cf}$  studied, but its regularity and qualitative appearance varies with  $VR$  and  $Re_{cf}$ .

The structures displayed in our photographs have been either directly observed or indirectly inferred previously in the literature (*cf.* references mentioned previously or elsewhere in this paper and also their reference lists). The dynamics of the structures' formation, however, has not been consistently explained, at least not in terms of the constraints imposed by vorticity generation mechanisms.



FIGURE 5: Wake vortices in side view. The smoke is initially in the crossflow boundary layer.  $VR = 4$ ,  $Re_{cf} = 3800$ .

### 3. SOURCES OF VORTICITY AND STRUCTURE FORMATION

Since the near field is dominated by several distinct types of vortical structures, it is of interest to try to understand their origin and formation. In particular, the source and subsequent dynamics of the vorticity leading to the structures presented in §2 are described here.

The vorticity equation for a Newtonian, barotropic, and incompressible flow with no body forces is given by

$$\frac{D\omega}{Dt} = \omega \cdot \nabla u + v \nabla^2 \omega, \quad (1)$$

where  $\omega = \nabla \times u$  is the vorticity. As is emphasized by Morton (1984), eqn. (1) does not explicitly contain any vorticity generation terms; it shows only that vorticity is convected, stretched, turned, and diffused. New vorticity can only enter a flow through imposed initial conditions and/or wall boundary conditions; there are no sources of new vorticity within the flow. This is a fundamental point when considering the formation of the wake structures in particular, as will be seen presently.

Defining the vorticity flux out of a wall as  $\hat{n} \cdot \tilde{J}_0$ , where  $\tilde{J}_0 = -v(\nabla \omega)_0$  is the vorticity flux tensor at the wall and  $\hat{n}$  is the wall-normal unit vector, it can be shown (Wu, Wu & Wu 1987) that for nonaccelerating and nonrotating surfaces

$$\rho \hat{n} \cdot \tilde{J}_0 = -\hat{n} \times (\nabla p)_0 - \hat{n} [\hat{n} \cdot (\nabla \times \tau_0)] + (\hat{n} \times \tau_0) \cdot \nabla \hat{n}. \quad (2)$$

The first term on the right-hand side of eqn. (2) represents the vorticity source term due to a wall pressure gradient. The second term accounts for the gradient of wall-normal vorticity due to a wall shear stress  $\tau_0$  with a nonzero  $\nabla \times \tau_0$  wall-normal component. Finally, the third term accounts for the effects of wall curvature transverse to the wall shear

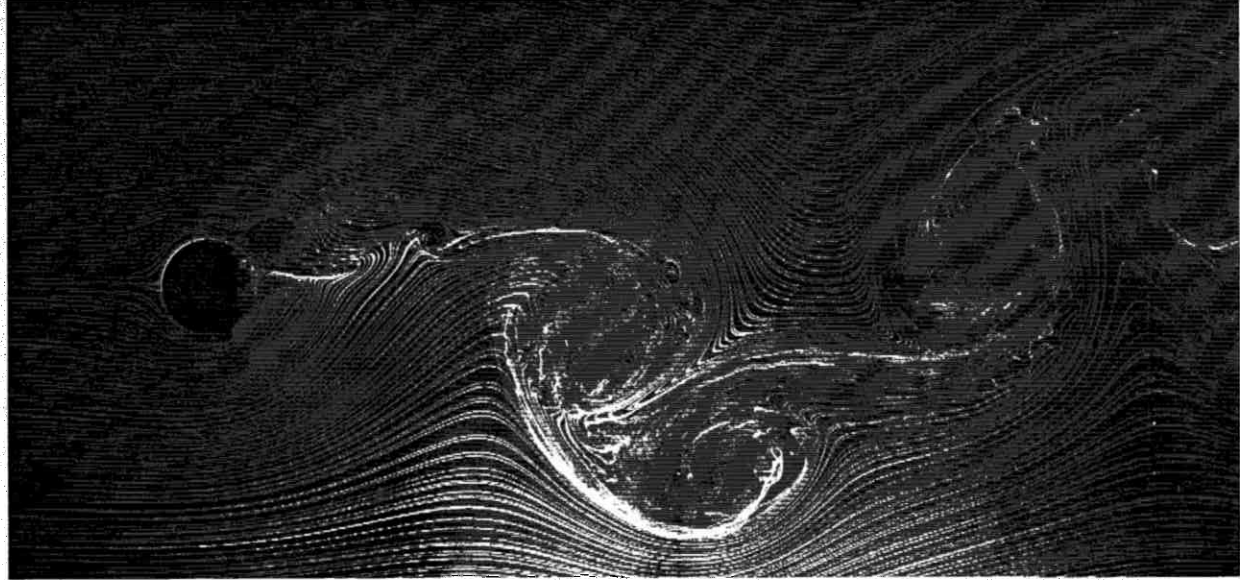


FIGURE 6: Wake vortices in cross section. The jet, near the left side of the photograph, issues directly at the viewer. The smoke-wire is at  $Z/D_j = .5$ .  $VR = 4$ ,  $Re_{cf} = 11400$ .

stress direction. With the above discussion in mind, the sources of vorticity for the four kinds of structures mentioned in §2 can be identified.

The source of the distorted ring vorticity of the jet is the boundary layer vorticity in the nozzle supplying the jet flow, again directly analogous to a free jet. The initial nearly axisymmetric shear layer leaving the jet becomes unstable and forms the ring-like vortices.

We believe that the counterrotating vortex pair evolves from the shear layer vorticity of the jet, *i.e.* its ultimate source is in the vorticity issuing from the nozzle. In fact, the numerical results of Coehlo & Hunt (1989) suggest that this process has already begun within the boundary layer of the nozzle; the effects of the crossflow are felt within the nozzle. From numerical results, Sykes, Lewellen & Parker (1986) have previously suggested that the jet's ring vorticity may evolve into the counterrotating pair.

The source of vorticity for the horseshoe structures is in the approaching crossflow boundary layer and the crossflow wall region near the jet. The separated crossflow boundary layer ahead of the jet supplies the horseshoes with vorticity, and in addition the horseshoe vortices induce pressure gradients on the wall, thereby generating more vorticity.

That no new vorticity can be generated within the flow is essential to the proper description of the wake formation. To our knowledge, in every paper in which the transverse jet's wake formation has been discussed previously, the wake vorticity has been described as vorticity "shed" from the jet and/or as vorticity due to a jet/crossflow interaction analogous to a solid cylinder/crossflow interaction. Since the jet does not offer the crossflow a solid surface on which to generate new vorticity, as a solid cylinder does, such analogies are physically wrong and lead to an incorrect explanation of the wake formation. As will be addressed in §4, the actual events leading to the appearance of vortices in the wake of the jet appear to be quite different and more complex.

#### 4. WAKE CHARACTERISTICS AND WAKE FORMATION MODEL

This section is devoted to the vortical structures in the jet's wake. The wake is especially interesting because, even though it is qualitatively similar in appearance to a circular cylinder wake, its formation must be very different. The vorticity which is shed from a solid cylinder is vorticity which was generated solely at the surface of the cylinder; the pressure gradient production term in eqn. (2) is responsible. There is no such mechanism in the present case of a flow around a jet, since there is no no-slip condition at the jet/crossflow interface. The vorticity in the jet's wake must be vorticity which originated at a solid boundary, either within the nozzle or at the crossflow wall.

To study the wake further, smoke from different sources was used to track fluid. Smoke is considered to be a suitable marker of vorticity for our purposes. Since the effective Schmidt number for smoke is large, vorticity

diffuses faster than smoke does; we assume that once the vorticity is tagged, the smoke marks the cores of vortices. In figure 7, the jet is tagged by seeding the jet supply with cigarette smoke. A well-defined jet body is seen with no presence of smoke nor, apparently, jet fluid in the wake. Conversely, when the crossflow boundary layer is tagged with smoke, as was seen in figure 5, most of the smoke ends up in the wake vortices. These results suggest that the jet vorticity does not contribute to the wake vorticity. Not only does the jet not act like a solid cylinder, not generating any new vorticity, it also does not shed any of its vorticity to the wake. Rather, the source of the wake vorticity is the crossflow boundary layer.

It is clearly of interest to determine whether the wake vortices convect with a characteristic (Sommerfeld) frequency. Accordingly, frequency measurements were made using a hot-wire anemometer placed in the wake of the jet. The values, shown in figure 8, are independent of the hot-wire's location in the wake. [The values of  $f_w$  were based on the measurement of 22 individual spectra obtained with an IBM 2582A spectrum analyzer.] In general, the spectral peaks  $f_w$  (dominant frequencies) are not as sharply defined here as they would be in the wake of a solid cylinder, and the values of  $S_t w$  are somewhat lower than they are for a circular cylinder wake at the same  $Re_{cf}$ . The sharpness of the spectral peaks varies considerably with  $VR$ , but for each  $Re_{cf}$  investigated, the sharpest peaks were recorded for  $3.5 \leq VR \leq 4.5$ . This is also the range of  $VR$  for which the values of  $S_t w$  appear to be independent of  $Re_{cf}$ . Our values of  $S_t w$  are in the same range as those measured by Moussa *et al.* (1977).

For the purpose of verifying the source of the wake vorticity, spectra were also taken near the region denoted by the arrows in figure 9, where smoke is tagging the crossflow

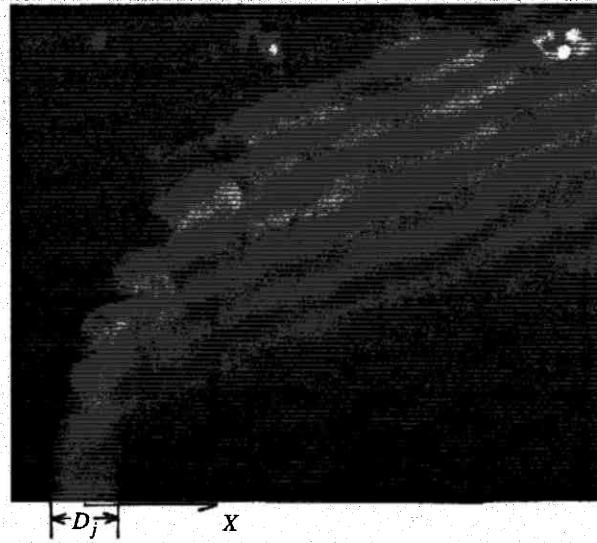


FIGURE 7: The jet, issuing from the bottom left-hand portion of the photograph, is tagged with smoke. This view is the same as in figure 5.  $VR = 4$ ,  $Re_{cf} = 3800$ .

boundary layer fluid. Upstream of the jet, a portion of the crossflow boundary layer separates and forms a horseshoe vortex. The boundary layer fluid outside the horseshoe structures on the jet's  $+Y$  side wraps around the jet and then separates on the its lee side, near the arrows in figure 9. The previous separation event, on the  $-Y$  side of the jet, has convected further downstream. Figure 10 shows the values for  $St_{sep}$  measured near such separation events; the agreement with Strouhal numbers measured in the wake is very good. Also, the sharpest spectral peaks are again seen for  $3.5 \leq VR \leq 4.5$ . These results support our conclusion that the source of the wake vorticity is in the crossflow boundary layer; that the characteristic frequencies of the separation events match those of the wake structures implies a connection between the two. The crossflow boundary layer separating at the downstream side of the jet to subsequently feed the wake is consistent with figure 5, where smoke seeding the crossflow boundary layer leaves

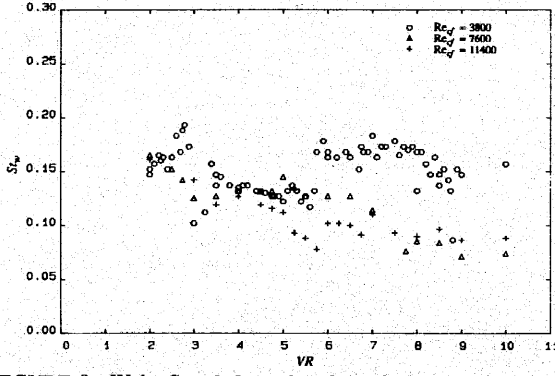


FIGURE 8: Wake Strouhal number dependence on velocity ratio at  $Re_{cf} = 3800$  (O), 7600 ( $\Delta$ ) and 11400 (+). Measured at  $X/D_j = 3.5$ ,  $Y/D_j = 1.5$ ,  $Z/D_j = .5$ .

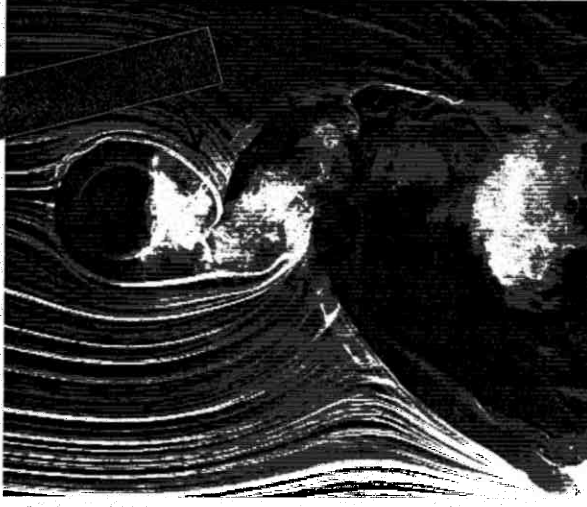


FIGURE 9: Separation event. A separation of the crossflow boundary layer is indicated by the arrows.  $VR = 4$ ,  $Re_{cf} = 3800$ .

the wall aft of the jet. We conclude that the crossflow boundary layer separation events represent the inception of the transverse jet's wake formation.

A striking difference between the wake of a cylinder and jet is evident when comparing figure 11 with 6. In both cases, the smoke-wire is located at  $Z/D_j = .5$  (or, equivalently,  $Z/D_c = .5$ ) and  $Re_{cf} = 11400$ . The flow around the jet in figure 6 looks nearly potential; the near wake streaklines are closed. Conversely, the flow around the cylinder separates, thereby opening the near wake. The potential-like streakline pattern around the jet has important implications for the crossflow boundary layer flow; the adverse pressure gradient on the lee side of the jet is imposed on the crossflow wall. This adverse pressure

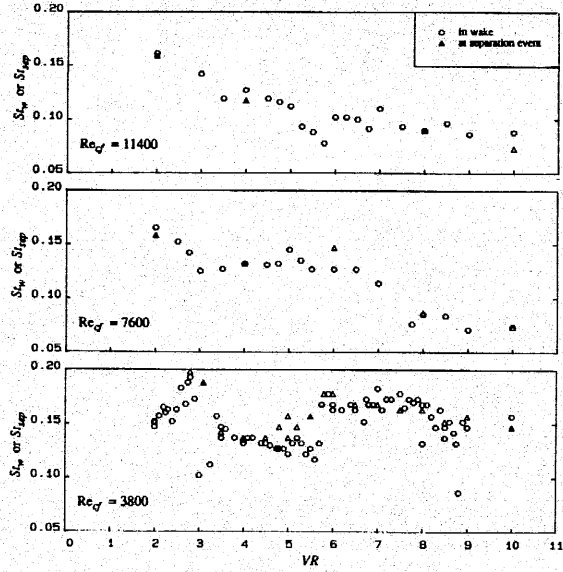


FIGURE 10: Comparison of wake (O) and separation events' ( $\Delta$ ) Strouhal numbers.  $St_{sep}$  measured near the cross-flow boundary layer separation events.  $St_w$  measured at  $X/D_j = 3.5$ ,  $Y/D_j = 1.5$ ,  $Z/D_j = .5$ .

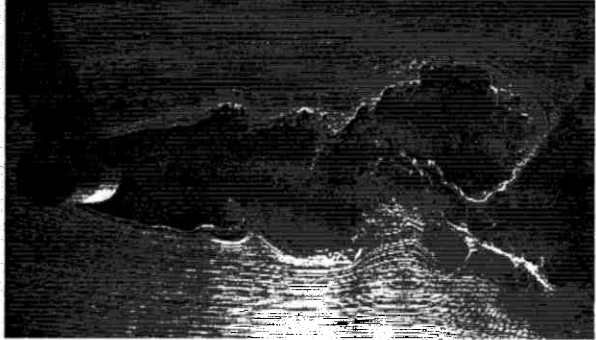


FIGURE 11: Circular cylinder wake in cross section. The cylinder is at the left end of the photograph. The aspect ratio of the wall-mounted cylinder is 6.  $Re_{cf} = 11400$ .

gradient is conducive to separating the crossflow boundary layer, near where the separation events have been identified. On the other hand, for the case of the cylinder, which has an open near wake, the crossflow boundary layer does not encounter such an adverse pressure gradient on the lee side; thus there is no analogous separation.

The model presented here for wake formation is based on the crossflow boundary layer separation events as described above. Once separation occurs, the vorticity from the crossflow boundary layer is free to convect, stretch, turn, and diffuse, as eqn. (1) shows. That portion closest to the jet is entrained and convected by the jet, thus establishing the connection of the wake vortices with the jet. As these newly formed structures convect downstream, they are free to stretch and turn to form a wake such as those seen in figures 5 and 6. In general, the separation events alternate from one side of the jet to the other with  $+Y$  crossflow boundary layer fluid feeding wake vorticity of  $-Z$  sense, and vice versa. The separation events, in all likelihood, represent only the inception of the wake structures. Vorticity near the wall can be continuously fed into the wake structures as they convect downstream. In addition to the vorticity already present in the crossflow boundary layer, new vorticity is undoubtedly generated due to the newly imposed fluctuating pressure gradients and rotational wall shear stress present at the crossflow wall (refer to eqn. (2)).

## 5. SUMMARY AND IMPLICATIONS

The principal message of this paper is the finding, which we believe is new, that the system of vortices in the wake of a transverse jet is distinctly different in origin and formation from the vortices which are shed from a solid cylinder. In the case of the transverse jet, where the jet/crossflow interface cannot generate new vorticity, the wake vorticity comes from the boundary layer on the wall from which the jet issues. The crossflow boundary layer separates on the downstream side of the jet because it cannot negotiate the adverse pressure gradient which is imposed on it by the flow around the jet, and its vorticity is incorporated into the wake vortices, which extend from the wall to the bending jet.

The mechanism which determines the frequency at which the wake vortices form is not clear but appears to be different from the shedding mechanism in a solid cylinder wake. The characteristic Strouhal number in the wake of a jet issuing from a wall was found to be consistently lower than that of a cylinder wake. It is of interest to compare the wake structure here to the corresponding case of a jet issuing from a pipe protruding into the crossflow. In the latter case, Moussa *et al.* (1977) have observed that the jet's wake frequency more closely matches the frequency of a cylinder wake. This implies that the vortex shedding from the pipe controls the structure in the jet's wake. In fact, it is consistent with our case to speculate that the vortices in the wake of a protruding jet are extensions of the vortices shed from the pipe, just as the vortices in the wake of a flush-mounted jet are extensions of vorticity from the crossflow

boundary layer.

Other problems of interest include the question of how the wake vortices interact with the other vortex structures: namely, the jet shear layer vortices, the horseshoe vortices, and the nascent far field vortex pair. Consequently, it is not clear whether the wake vortex system (as well as the horseshoe vortex system) has a strong effect on the development of the main jet flow.

That the wake vorticity comes from the crossflow boundary layer fluid and not from the jet fluid is of importance when considering the mixing in this flow. The results suggest that the wake does not add substantially to the mixing of ambient (crossflow) fluid with jet fluid; the wake contains essentially no jet fluid. Broadwell and Breidenthal (1984) note that the transverse jet appears to be a better mixer of jet and ambient fluid than a free jet. The present results imply that the wake may not contribute to this enhanced mixing. The results also suggest that it may be possible to efficiently mix fluid near or in the crossflow boundary layer with the mean crossflow by taking advantage of the wake formation dynamics.

**Acknowledgements:** We would like to thank Professor H.G. Hornung for many helpful discussions on the issue of vorticity generation. This work was partially supported by ONR contract #N00014-85-K-0646.

## REFERENCES

- BROADWELL, J.E. & BREIDENTHAL, R.E. 1984 Structure and mixing of a transverse jet in incompressible flow. *J. Fluid Mech.* **148**, 405-412.
- COEHLHO, S.L.V. & HUNT, J.C.R. 1989 The dynamics of the ← near field of strong jets in crossflows. *J. Fluid Mech.* **200**, 95-120.
- CORKE, T., KOGA, D., DRUBKA, R. & NAGIB, H. 1977 A new technique for introducing controlled sheets of streaklines in wind tunnels. *IEEE Publication 77-CH1251-8 AES*.
- FEARN, R. & WESTON, R.P. 1974 Vorticity associated with a jet in a cross flow. *AIAA J.* **12**, 1666-1671.
- FOSS, J.F. 1980 Interaction region phenomena for the jet in a cross-flow problem. *Rep. SFB 80/E/161*, University of Karlsruhe.
- KARAGOZIAN, A.R. & GREBER, I. 1984 An analytical model for the vorticity associated with a transverse jet. *AIAA 17th Fluid Dyn., Plas. Dyn. & Las. Conf.*
- KUZCO, D.M. & ROSHKO, A. 1984 Observations on the wake region of the transverse jet. *Bulletin of the American Physical Society*, **29**, 1536.
- MCMAHON, H.M., HESTER, D.D. & PALFREY, J.G. 1971 Vortex shedding from a turbulent jet in a cross-wind. *J. Fluid Mech.* **48**, 73-80.
- MORTON, B.R. 1984 The generation and decay of vorticity. *Geophys. Astrophys. Fluid Dyn.* **28**, 277-308.
- MOUSSA, Z.M., TRISCHKA, J.W. & ESKINAZI, S. 1977 The near field in the mixing of a round jet with a cross-stream. *J. Fluid Mech.* **80**, 49-80.
- SYKES, R.I., LEWELLEN, W.S. & PARKER, S.F. 1986 On the vorticity dynamics of a turbulent jet in a crossflow. *J. Fluid Mech.* **168**, 393-413.
- WU, J.Z., WU, J.M. & WU, C.J. 1987 A general 3-dimensional viscous compressible theory on the interaction of solid body and vorticity-dilation field. UTSI Report 87/03.